

AD _____

Award Number: W81XWH-11-1-0121

TITLE: Noninvasive Spatially Offset and Transmission Raman Mapping of Breast
Tissue: A Multimodal Approach Towards the In Vivo assessment of Tissue Pathology

PRINCIPAL INVESTIGATOR: Matthew Schulmerich

CONTRACTING ORGANIZATION: University of Illinois
Urbana, IL 61801

REPORT DATE: April 2013

TYPE OF REPORT: Annual Summary

PREPARED FOR: U.S. Army Medical Research and Materiel Command
Fort Detrick, Maryland 21702-5012

DISTRIBUTION STATEMENT: Approved for Public Release;
Distribution Unlimited

The views, opinions and/or findings contained in this report are those of the author(s) and should not be construed as an official Department of the Army position, policy or decision unless so designated by other documentation.

REPORT DOCUMENTATION PAGE

*Form Approved
OMB No. 0704-0188*

Public reporting burden for this collection of information is estimated to average 1 hour per response, including the time for reviewing instructions, searching existing data sources, gathering and maintaining the data needed, and completing and reviewing this collection of information. Send comments regarding this burden estimate or any other aspect of this collection of information, including suggestions for reducing this burden to Department of Defense, Washington Headquarters Services, Directorate for Information Operations and Reports (0704-0188), 1215 Jefferson Davis Highway, Suite 1204, Arlington, VA 22202-4302. Respondents should be aware that notwithstanding any other provision of law, no person shall be subject to any penalty for failing to comply with a collection of information if it does not display a currently valid OMB control number. PLEASE DO NOT RETURN YOUR FORM TO THE ABOVE ADDRESS.

1. REPORT DATE April 2013			2. REPORT TYPE Annual Summary			3. DATES COVERED 1 April 2012 – 31 March 2013		
4. TITLE AND SUBTITLE Noninvasive Spatially Offset and Transmission Raman Mapping of Breast Tissue: A Multimodal Approach Towards the In Vivo assessment of Tissue Pathology			5a. CONTRACT NUMBER					
			5b. GRANT NUMBER W81XWH-11-1-0121					
			5c. PROGRAM ELEMENT NUMBER					
6. AUTHOR(S) Matthew Schulmerich E-Mail: schulmer@illinois.edu			5d. PROJECT NUMBER					
			5e. TASK NUMBER					
			5f. WORK UNIT NUMBER					
7. PERFORMING ORGANIZATION NAME(S) AND ADDRESS(ES) University of Illinois Urbana, IL 61801			8. PERFORMING ORGANIZATION REPORT NUMBER					
			10. SPONSOR/MONITOR'S ACRONYM(S)					
9. SPONSORING / MONITORING AGENCY NAME(S) AND ADDRESS(ES) U.S. Army Medical Research and Materiel Command Fort Detrick, Maryland 21702-5012			11. SPONSOR/MONITOR'S REPORT NUMBER(S)					
			12. DISTRIBUTION / AVAILABILITY STATEMENT Approved for Public Release; Distribution Unlimited					
13. SUPPLEMENTARY NOTES								
14. ABSTRACT The purpose of this research project is to develop new approaches that can impact early diagnosis of breast cancer, post-biopsy analysis, lymph node examinations, and drug delivery studies. The scope of this training involves optimizing Raman instrumentation and methods for efficient illumination and collection of Raman scattered light originating from deep within breast tissue. Experiments encompass designing tissue phantoms using Intralipid®, dyes/pigments, inclusions, and agarose gel to quantitatively characterize the instruments' capabilities and performance. Additionally, we conduct spectroscopy on tissue biopsies to correlate spectral bands with healthy and diseased breast tissue. Observed spectral changes are compared to infrared images and H&E/HIS-stained images to relate observed biochemical changes to histology. The Raman data will be used to generate and train classification algorithms for automated histopathology as a starting point for in vivo work at the culmination of this training program. This report outlines progress for year 1 of the 3 year training program. In the approved statement of work 5 tasks were stated. All 5 tasks were successfully completed. We now have a working relationship with local clinicians. We have built-up a comprehensive database consisting of micrographs and IR spectral images for identify breast tissue histology and tissue chemistry. We have acquired Raman measurements on biopsied tissue. We have identified Raman spectral bands that can be used for distinguishing between different tissue types and have applied those Raman spectral bands to achieve cell-level contrast in Raman spectral images. Additionally, we have used clinical observations and interaction with clinicians to develop a conceptual design for a Raman Tomography instrument aimed at breast cancer screening. Finally for Raman tomographic reconstruction, we have evaluated existing diffuse optical tomography algorithms specifically for Raman measurements and have adapted a Monte Carlo framework for our Raman tomographic reconstruction. Through modeling and experimentation we characterized different instrument configurations and have implemented the transmission fan style configuration into our prototype instrument design which uses fiber-optics in-contact with tissue to give the maximum collection efficiency.								
15. SUBJECT TERMS Raman Spectroscopy, Breast Cancer, SORS, Transmission spectroscopy, Raman Tomography, Raman Imaging, Infrared Imaging								
16. SECURITY CLASSIFICATION OF:			17. LIMITATION OF ABSTRACT UU	18. NUMBER OF PAGES 37	19a. NAME OF RESPONSIBLE PERSON USAMRMC			
a. REPORT U	b. ABSTRACT U	c. THIS PAGE U				19b. TELEPHONE NUMBER (include area code)		

Table of Contents

	<u>Page</u>
Introduction.....	4
Body.....	5
Key Research Accomplishments.....	16
Reportable Outcomes.....	16
Conclusion.....	17
References.....	18
Appendices.....	19

INTRODUCTION: The **subject** of this research is to develop non-invasive optical instrumentation and methods for obtaining chemical contrast from deep within breast tissue. The overarching goal of this training program is to become steeped in breast cancer clinical practice and research to independently develop a new technology from a concept. My learning objectives include the following: first, fill in the gaps in my basic knowledge of breast cancer and pathology. Second, build a knowledge base as to the chemical changes that are occurring within breast tissue and how those changes are reflected in the vibrational spectra. Third, to understand the optics of breast tissue to gain most efficient illumination and collection schemes for instrumental design. The **purpose** of this research project is to develop new approaches that can impact early diagnosis of breast cancer, post-biopsy analysis, lymph node examinations, and drug delivery studies. Additionally, this technology could be used to study animal models for tissue engineering, 3D tissue scaffolds and has a variety of other basic research as well as clinical applications. The **scope** of this training involves optimizing Raman instrumentation and methods for efficient illumination and collection of Raman scattered light originating from deep within breast tissue. Experiments encompass designing tissue phantoms using Intralipid®, dyes/pigments, inclusions, and agarose gel to quantitatively characterize the instruments' capabilities and performance. Additionally, we conduct spectroscopy on tissue biopsies to correlate spectral bands with healthy and diseased breast tissue. Observed spectral changes are compared to infrared images and H&E/HIS-stained images to relate observed biochemical changes to histology. The Raman data will be used to generate and train classification algorithms for automated histopathology as a starting point for *in vivo* work at the culmination of this training program.

BODY: The approved statement of work is illustrated in figure 1. For year two, four tasks were outlined. Details of the work conducted in year two are present on the following pages.



Figure 1) Summary figure and timeline for approved statement of work

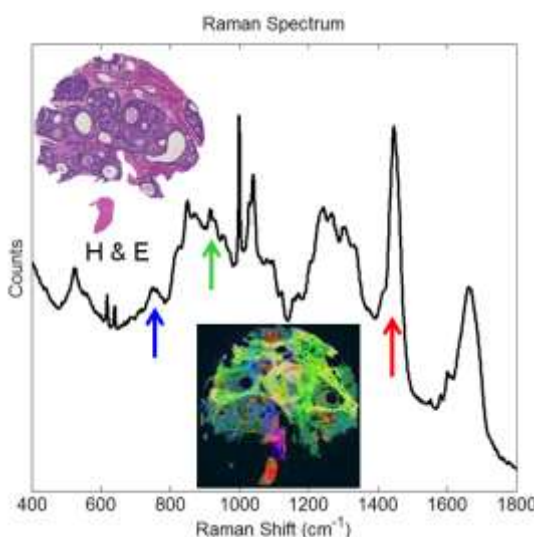


Figure 2) Raman image of a breast tissue biopsy and corresponding H&E Serial section

Task 1.4 Justification of correlations (month 13-18):

This task was successfully completed. Data from year 1 was analyzed and additional Raman images were acquired to further understand the complex Raman signal observed from the different cell types that make-up breast tissue. Through Raman imaging the chemical contrast achieved through various spectral bands is apparent. The Raman image displayed in figure 2 is comprised of a red, green, and blue pixels corresponding to the intensities of 3 Raman bands (781 cm^{-1} shift in blue, 936 cm^{-1} shift in green, and 1450 cm^{-1} shift in red.) The contrast observed in an H&E serial section is mirrored in the Raman image. The challenge lies in identifying the different tissue types and then comparing the different Raman signals to determine the spectral source of the contrast. While a first pass at identifying this contrast was completed in year 1, here the additional imaging experiments are in support of these results

By acquiring a Raman image and then observing histological stains of serial sections we can choose pixels

that are over the desired cell-types. As a simple example, we are able to distinguish epithelium from stromal tissue by masking-out only the tissue type of interest and then looking at the Raman spectrum of only that tissue type. This approach is illustrated in figure 3. We first collect a Raman image and then compare it to a serial section stained with H&E. The serial section allows us to identify which tissue structures are present in the Raman image. We then identify and mark the pixels that correspond to epithelium and to stromal tissue. We are able to then categorize all the spectra that are associated with stromal tissue and all the spectra that are associated with epithelial tissue and thus compare the differences in the spectra and compare that to the literature.^{1,2}

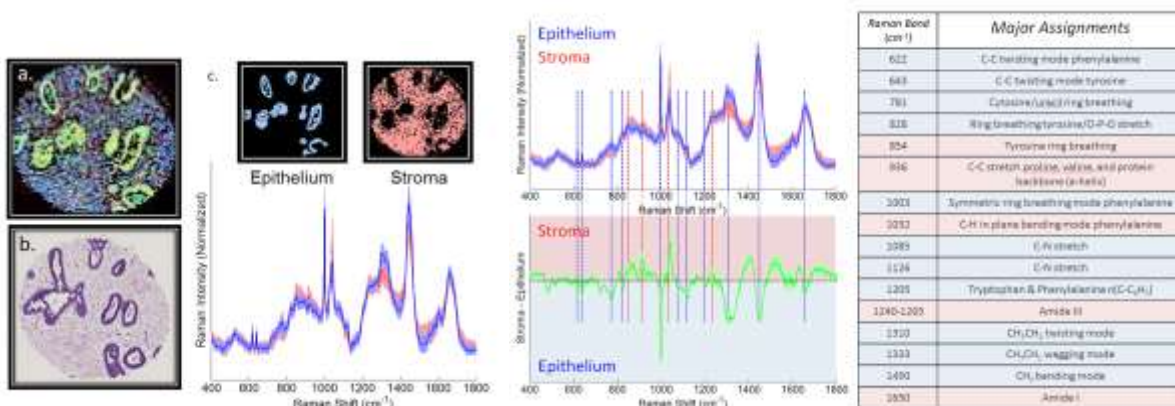


Figure 3) a. Raman image from an unstained tissue biopsy b. serial section H&E c. corresponding cell type masks and spatially recovered spectra along with the difference spectra (green) and band assignments

While the spatial distribution of epithelium and stromal tissue is of diagnostics importance, the clinical utility of imaging these two components alone is not significant. A significant tissue with diagnostic utility is myoepithelium.^{3,4} As depicted in figure 4, myoepithelium is comprised of a mesh-like network that surrounds lobules and ducts. These cells have the ability to contract in order to secrete milk from the lobule into the duct.

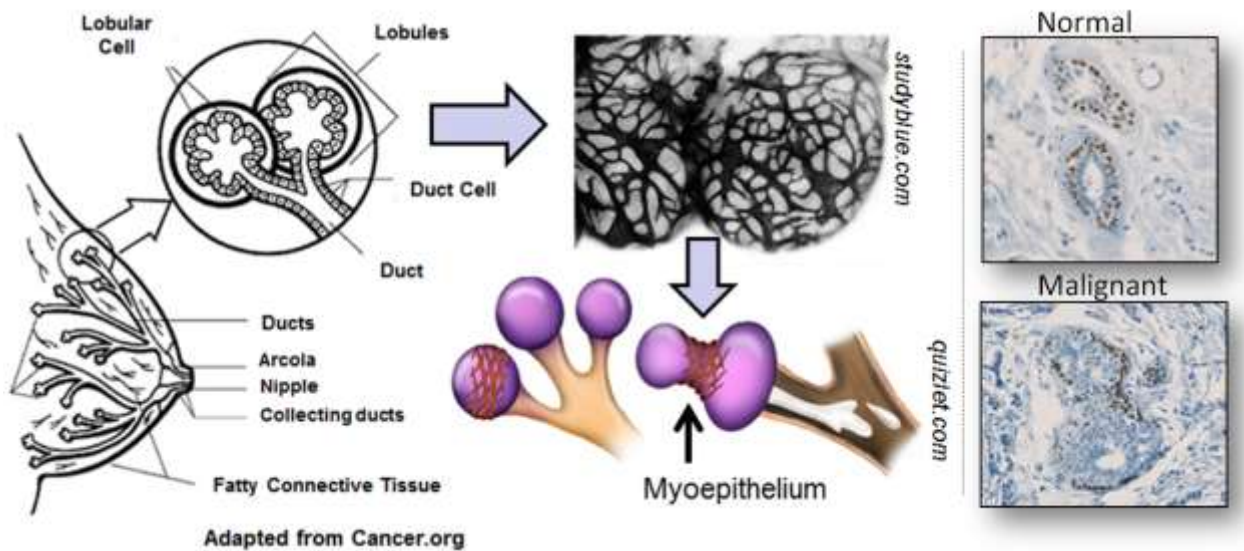


Figure 4) *left* Breast anatomy highlighting myoepithelium cells *right* P63 stained tissue illustrating the breakdown of the myoepithelial wall in a malignant cancer. The Myoepithelial cells are stained as dark brown.

They are present in healthy breast tissue even if a woman is not lactating. Myoepithelial cells are on the order of 1-2 micrometers thick and are not visualized with H&E staining. These cells are a main diagnostic marker for determining whether suspect tissue is benign or malignant. A pathologist will use the immunohistochemical stain P63 to specifically visualize these cell types.⁵ A P63 stain of normal vs malignant lesion is illustrated in 4. Myoepithelial cells are stained a dark brown color. The normal tissue has a continuous layer of myoepithelial tissue surrounding the lobules. In the malignant case, the myoepithelial layer is discontinuous and this would be diagnosed as an invasive carcinoma.

Using the same masking approach described in figure 3. We collected high resolution images of a biopsy section to determine if Raman spectroscopy has the chemical contrast to be able to discern myoepithelial tissue from epithelium and stromal tissue. From the comparison of Raman spectra between masked regions several bands of contrast are evident. In figure 5, the masked regions were determined by looking at H&E, P63, and SMA stained serial sections. The Raman spectra were then averaged between the marked sections to identify differences in the spectra. To visualize the chemical distribution within the tissue, three bands were chosen and those pixels were marked as red, green, and blue pixels. The resulting Raman image shows the contrast achieved by these 3 spectral bands. The resulting image is segmented well into the three components highlighted by the stained tissue. This figure demonstrates

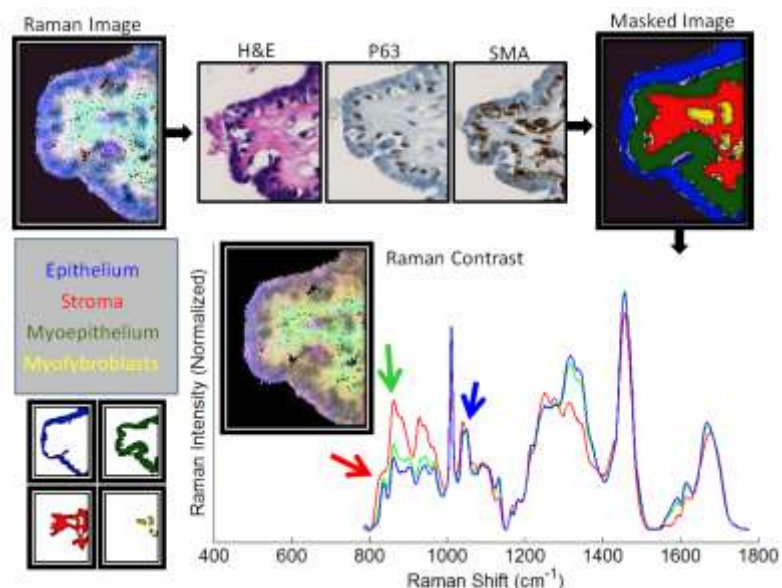


Figure 5) Approach to determining spectral contrast related to myoepithelium

the ability to obtain label free contrast of myoepithelial cells using Raman spectroscopy. This is an exciting prospect because Raman is conducive to in vivo measurements and the identification/quantification of myoepithelium is an extremely important diagnostic marker. We have sufficient data with spontaneous Raman to put together a manuscript; however we aim to increase our statistical power by increasing our image data-set using a higher speed complimentary technique.

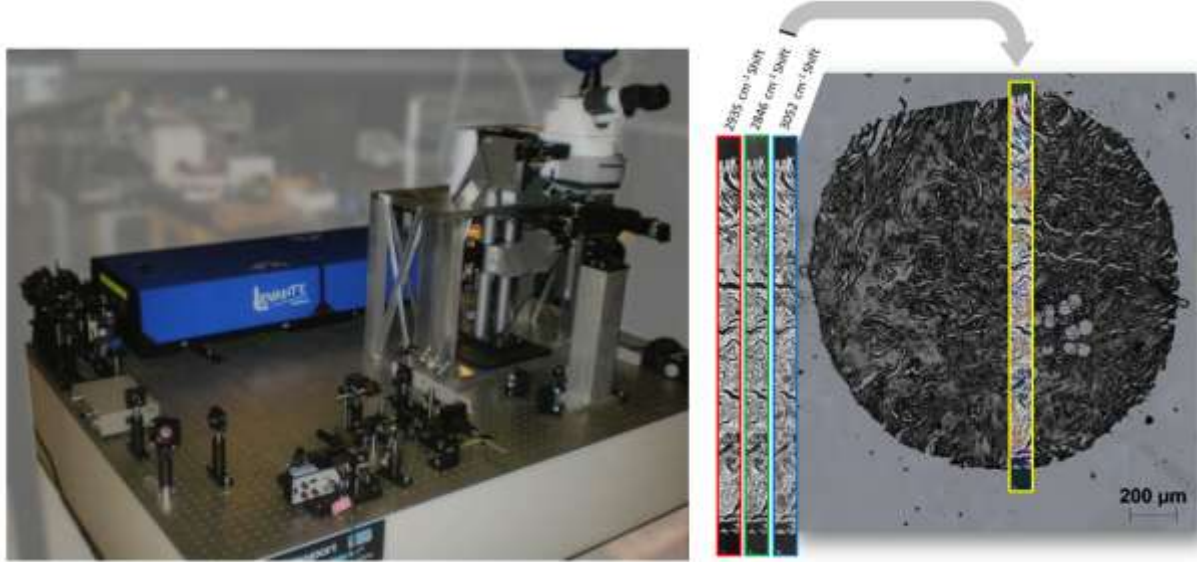


Figure 6) Preliminary data for future work made possible by the study we report here

To explore myoepithelial band assignments further, as future work, we are interested in collecting large images of multiple biopsy sections using stimulated Raman spectroscopy (SRS)^{6,7}. The information gained from the spontaneous Raman imaging give us insight into which spectral bands are worth pursuing in order to gain cellular/tissue type contrast. With SRS imaging we are able to collect large image areas on the order of 1mm squared in about one hour per band. This same size would take days to weeks with spontaneous Raman approaches severely limiting the practical statistical power we can achieve. However before one is able to do SRS it is important to know which spectral bands will give chemical contrast. The spontaneous Raman images presented above along with some others we have collected give us a good starting point to conduct an SRS study. As a first step towards this effort we have built and are currently optimizing an SRS microscope for the evaluation of Breast tissue. A photo of this instrument and some preliminary data are depicted in figure 6.

Task 1.5 Classification Algorithm (month 19-30):

To complement the Raman data that was acquired, Mid-IR Spectroscopy was used to develop classification algorithms⁸. Similar to the Raman approach, stains were employed to identify regions of pathological significance. A modified Bayesian classification algorithm was used with spectral metrics to calibrate a transfer function on identifying epithelial cells, fibroblast rich stroma, collagen rich stroma, myofibroblast rich stroma, blood, necrosis, lymphocytes, and mucin pixels. Multiple students and postdocs worked on developing this classification algorithm and to-date we have trained on ca.250 breast tissue biopsy specimen and validated on an additional ca.250 breast tissue biopsy specimen. Early results from the validation set are presented in figure 7. Training was performed by taking a 5μm tissue section for FT-IR imaging and then taking serial sections which were stained using multiple special and IHC stains. IR pixels corresponding to deduced cell types were identified (>500,000 pixels) for training. This was further validated on an entirely separate cohort of over 200 patients. An average Area Under the Curve (AUC) for cell type classification of 0.93 using 33 spectral-metrics was achieved in the training array and 0.91 AUC for the validation array. Figure 7, demonstrates the potential of FT-IR imaging coupled with this Bayesian classifier to reduce the burden on the pathologist with the ability to accurately classify the cell types in the example core from

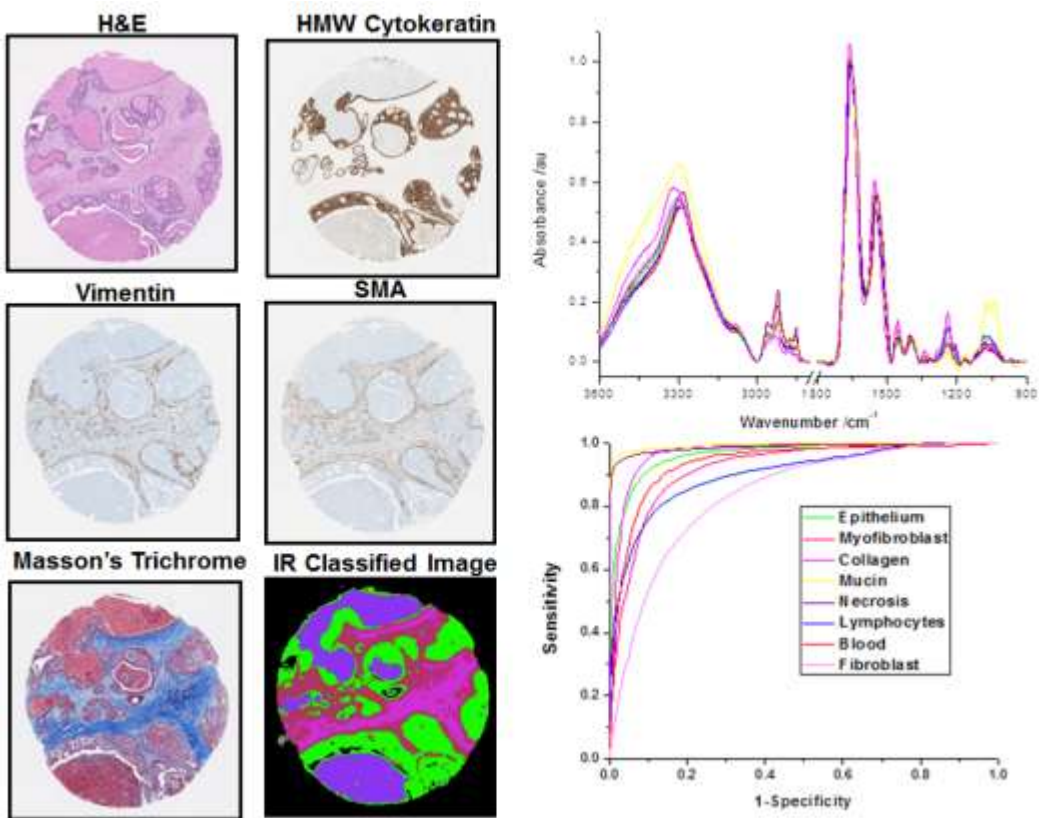


Figure 7) Example of a Bayesian tissue classification result and the validation results

a single unstained IR classified tissue section. To otherwise identify the cell types within this example core would have involved a panel of 5 stains to be performed with the pathologist then deducing cell types based on the pattern of positive and negative staining.

With this imaging technology, one aim is to improve or classification accuracy. However we are limited by the spatial resolution of our instrumentation. Some of my effort was spent improving the optics and alignment of our FTIR imaging instrumentation⁹. The results from this work successfully improve our classification accuracy as we are able to obtain proper sampling of the specimen in the microscopes field of view. Figure 8 illustrates the improved classification as highlighted by the red arrows. In this figure the green pixels have been classified as epithelium and the pink pixels have been classified as stromal tissue. By improving the spatial resolution the structure of the tissue-type distribution becomes clearer and will lead to more accurate diagnosis. For example in figure 8, the standard IR approach leads to the appearance of masses of epithelium. A mass of epithelium tissue generally warrants a closer look, such as additional staining to look for the presence or absence of myoepithelial cells. However, on inspection of the HDIR image the tissue looks normal and there would be no need for further investigation as the epithelial cells are simply part of a terminal ductal lobular unit that are a normal part of breast anatomy.

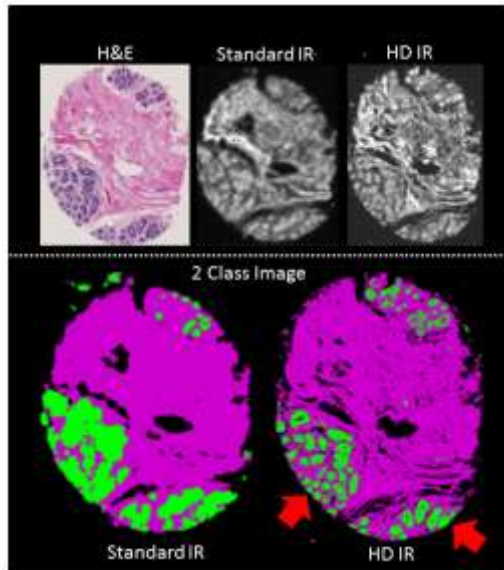


Figure 8) High Definition IR imaging leads to better classification

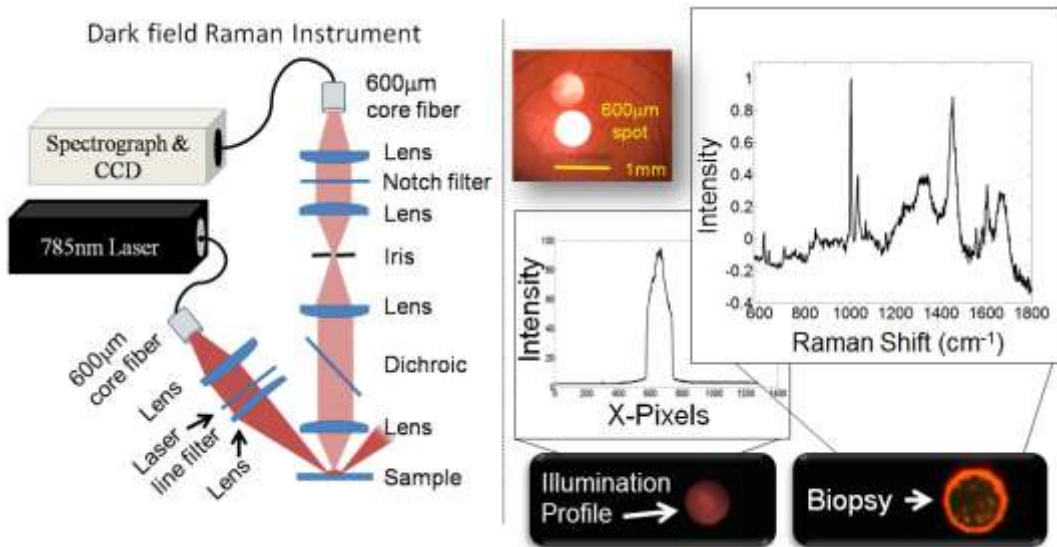


Figure 9) Dark field Raman schematic and characterization for large spot Raman spectroscopy of tissue biopsies

This tissue type classification algorithm that we have developed and validated is extremely useful for Raman experiments to look into the classification accuracy of Raman spectroscopy which is something we will need to understand as we progress into *in vivo* work with Raman. Towards the development of a Raman classification model we have built an instrument to collect a single Raman spectrum form a millimeter or smaller sectioned biopsy specimen. The IR classification model described above is used as a reference to determine the number of cell types that are present for a given core specimen. We can then use that information to train an algorithm to quantify the number of cell types that exist under the Raman field of view. In addition to training for cell types that are present we are also able to train for disease states, ie hyperplasia, dysplasia, malignant, benign.

The instrumentation has been built and characterized using archived tissue that was present in the lab from completed experiments. A schematic of the instrument is depicted in figure 9. The Raman excitation is incident at angles oblique to the collection optics. The leads to only collecting Raman signal from the scattered light and as a result rejects the subsurface signal¹⁰. In the configuration presented here we adjusted the collection aperture to

collect light from a spot size of 600 micrometers. We have also optimized the system for collection from a 1mm biopsy specimen. The data in figure 9 shows the illumination profile, which we would want to be as top-hat shaped as possible, along with the Raman spectrum of a biopsy section placed in this profile.

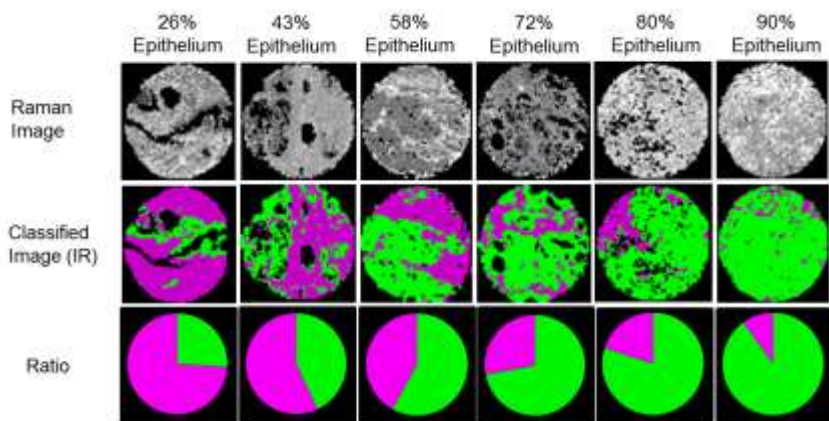


Figure 10) (top) Raman images of biopsy specimens with varying ratios of epithelium and stromal tissue (middle) classified IR images illustrating the distribution of epithelium and stromal tissue. (bottom) the ratio of epithelium and stromal tissue quantified by the IR classification

The information we anticipate to obtain from this single Raman spectrum is illustrated in figure 10. While one approach is to collect images and understand the distribution of tissue in order to diagnose disease, perhaps simply obtaining the representative chemical

information is enough as this would be the type of information obtained with Raman tomography as the technique has low spatial resolution, but high chemical specificity. Therefore, by using the IR images and classification algorithm described in figure 7, we can quantify the percentage of epithelium as compared to total area of the image giving us an epithelium to stromal tissue ratio. With this ratio as a reference value we are able to develop a transfer function that will take an input a Raman spectrum and calculate the percentage of epithelium in the core it was collected from. Some preliminary results for this technique are presented in figure 11. A leave-one-out cross-validation model was employed to evaluate the technique's ability to quantify multiple cores for epithelium. In this example we are able classify a biopsy core for the % epithelium with an error of about 13%. Work is currently underway with a larger sample size to quantify biopsy cores for the 8 tissue types described in the classifier above (figure7). In addition evaluating tissue types we are also using this approach to classify disease diagnosis. This work is currently underway.

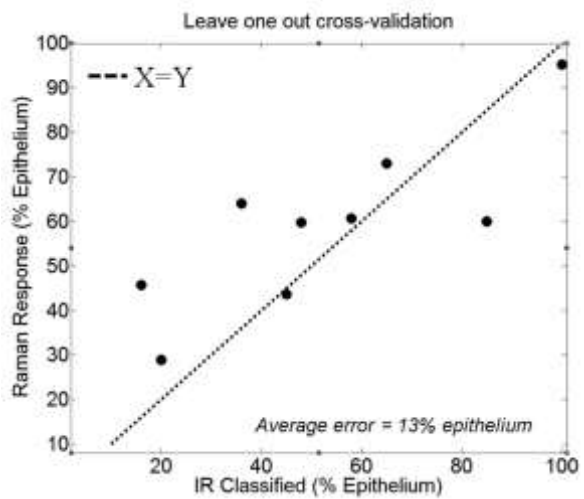


Figure 11) Single spectrum Raman calibration model for predicting %epithelium from a biopsy specimen

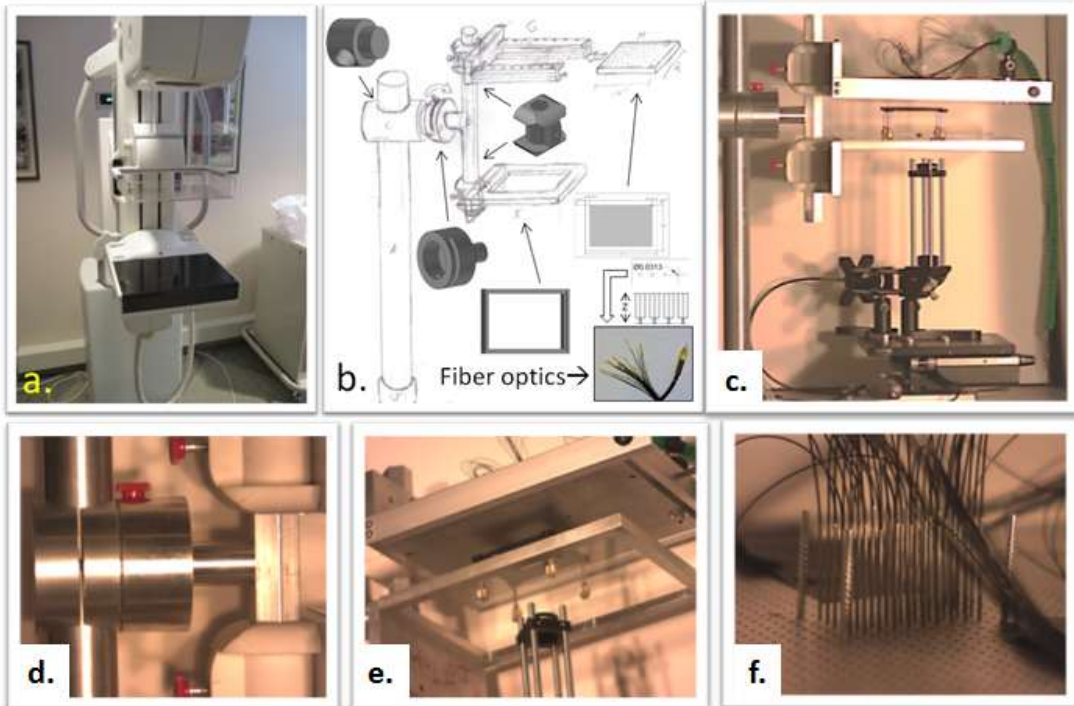


Figure 12) a) Photo taken at Provena Covenant Medical Center of a mammogram instrument b) Conceptual design and AutoCAD files for a breast cancer screening Raman instrument c) a photograph of the prototype instrument d) 0-90 degree hinge and adjustable paddles e) View looking up from the bottom plate f) collection fibers

Task 2.3 Construction of Instrumentation and calibration standards (month 13-18): All major instrumentation and components have been purchased and are assembled. The Raman tomography instrument design is depicted in

figure 12a and 12b (this is the same figure reported in the year 1 updated). Photographs of the constructed instrument are now included in figures 12c-12f. The Raman excitation light enters into the sample at the bottom plate (figure 12e). After the excitation light travels through the sample it is collected by the optical fibers that can be freely arranged for mapping purposes. The illumination arm is also freely adjustable and is combined with automated translation stages for control in the x and y dimension. The depicted instrument configuration illuminates all 50 fibers independently resulting in 2500 spectra all with known coordinates for illumination and collection. The light from the collection fiber travels to a Raman spectrograph as depicted in figure 13.

At the spectrograph the fibers are transposed into a line and the collected light travels through a pre-stage notch filter. The collected light is then focused through a 100x1000 micrometer slit and is then collimated. Finally, the signal is dispersed onto a CCD. The spectrograph depicted in figure 13 was modified to include a home-built internal illumination source. This is a white-light LED with a pull lever that allows us to illuminate through the fibers to see where the collection regions will be on the sample. This is useful in sample alignment. For each fiber

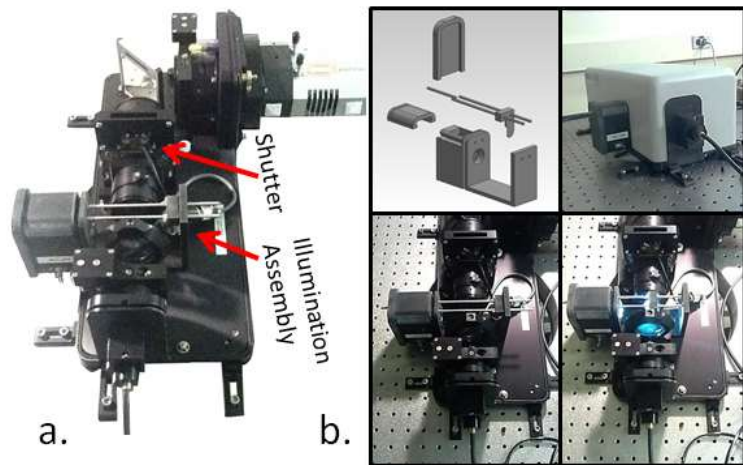


Figure 13) a) Modified spectrograph b) Solid works rendering and photos of the illumination assembly

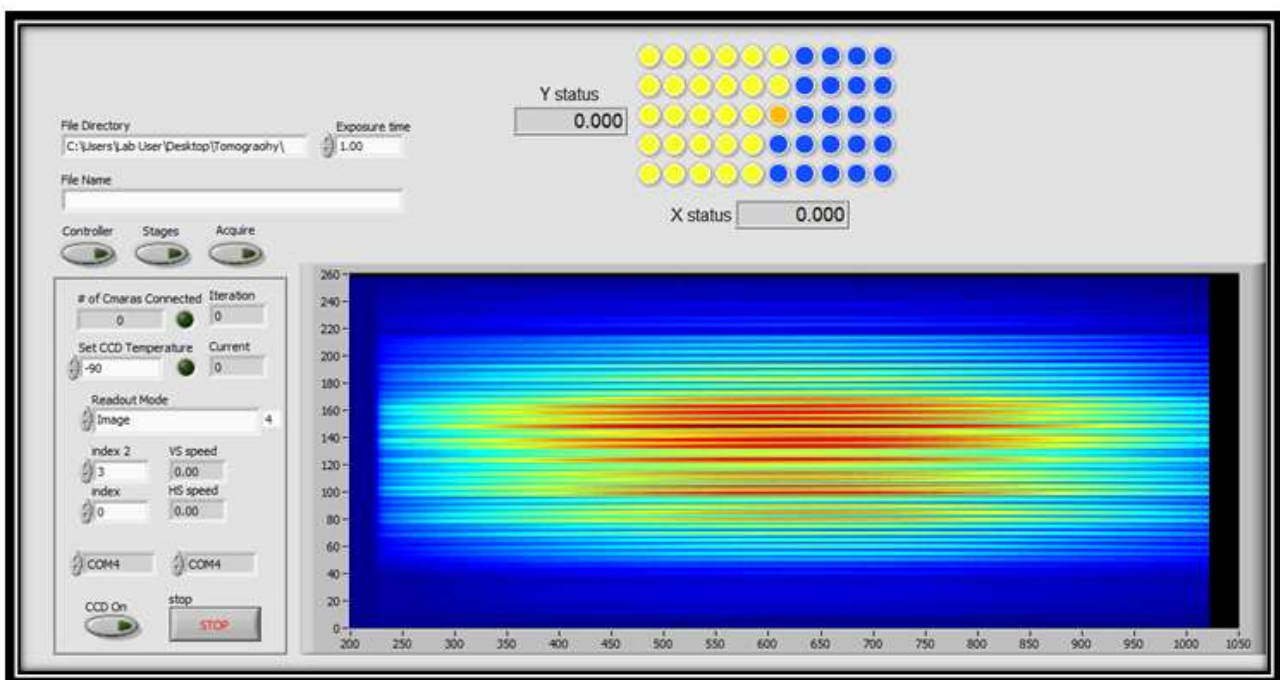


Figure 14) Screenshot of LabView front panel and data collected from white light illumination of all fibers

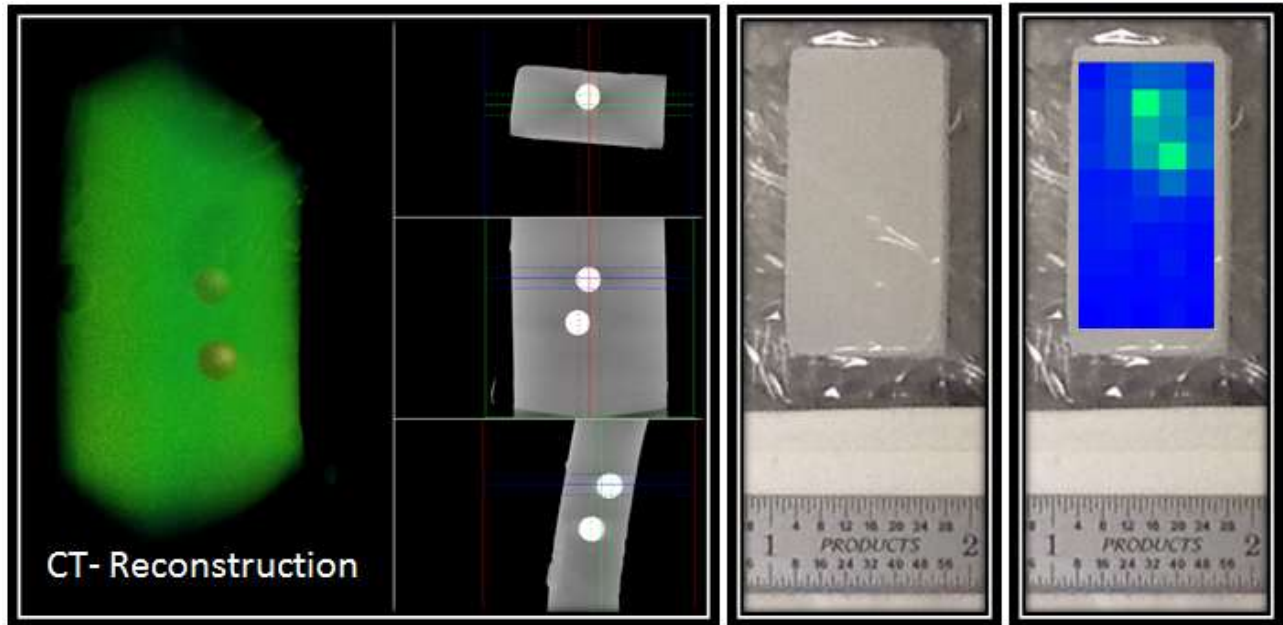


Figure 15) (left) a computed tomography reconstruction of an Intralipid tissue phantom (center) and image of the tissue phantom (right) a transmission Raman pixel map collected with the instrument depicted in figure 12 illustrating the location of the Teflon inclusions

we have mapped the positional correspondence of where the fiber is on the top paddle grid and where the fiber enters the spectrograph. The entire instrument is controlled by LabView and is now completely automated. A screen shot of the current LabView front panel and a CCD frame of all the fibers is illustrated in figure 14. A sample can be put into the instrument and the illumination point will be translated according to the specified stage coordinates. The Completed positions are then marked as yellow, the current position is marked as orange, and the future positions are marked in blue.

To aid in aligning the tomography instrument and processing the resulting data, simple Intralipid and agar phantoms were fabricated. As an example the phantom in figure 15 was an agar phantom with 0.1% Intralipid dispersed through the agar. The target for this phantom was two Teflon sphere place 3mm apart. We verified the location of the spheres using computed tomography. The center image of figure 15 depicts a photograph of the Intralipid phantom and it is clear that the two spheres are not visible. We then put the phantom on the tomography instrument and mapped-out the fiber signals. It is clear from figure 15 that the location of the spheres has been determined by the Raman instrument. A manuscript is preparation for this work and we are currently optimizing our reconstruction methods for the new instrument design.

Task 2.4 Collect data using more realistic tissue phantoms (month 19-24):

Tissue phantoms with a reasonable shelf life (1-2weeks) and more geometrical accuracy are important steps to developing and characterizing the tomography instrument. This has proved challenging. As depicted in figure 15, we observe two

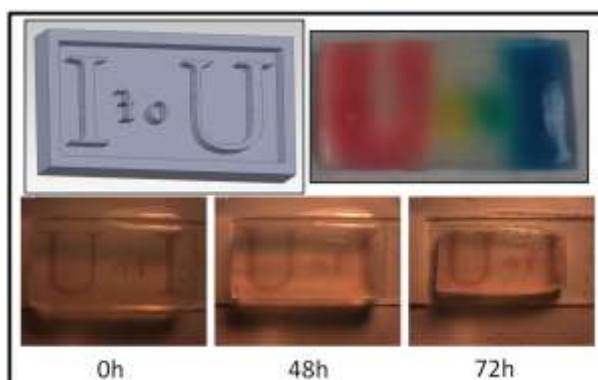


Figure 16) U of I tissue phantom to investigate storage conditions and shelf-life

significant problems. The first is that the phantoms evaporate quickly resulting in a change in their dimensions and optical properties. Second, any liquid inclusions, such as dyes, pigments, or nanoparticles, tend to diffuse and spread-out throughout the phantom thus blurring any structure intentionally introduced into the phantom. Several experiments are currently underway to investigate approaches to mitigating these two experimental challenges. To-date we have been able to make the evaporation no-long an issue. We simply vacuum seal the phantom in a thin polyethylene film. This preserves the phantom's structure and does not interfere with the Raman signal. The diffusion of liquid inclusions is still an on-going challenge. We have considered including 3-D printed sugar structures as inclusions to avoid the use of liquids.

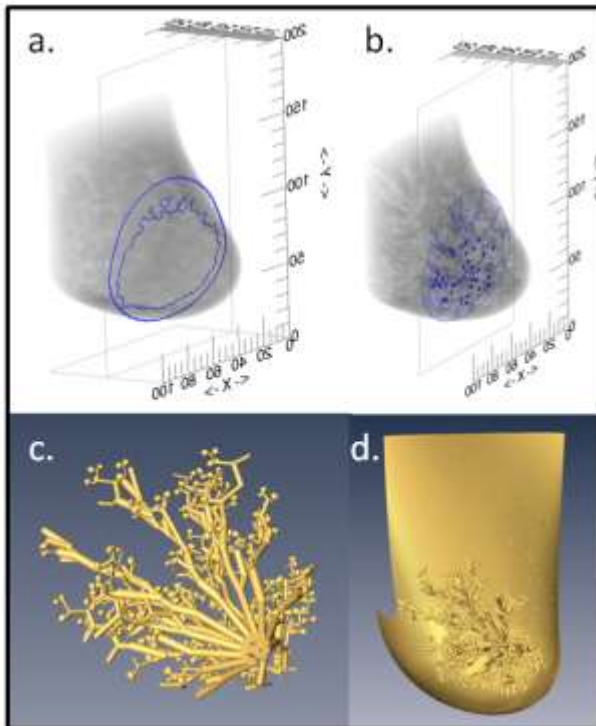


Figure 17) a) IDL in silico model b) IDL in silico model highlighting ductal structures c) Isolated ductal system d) Breast phantom model

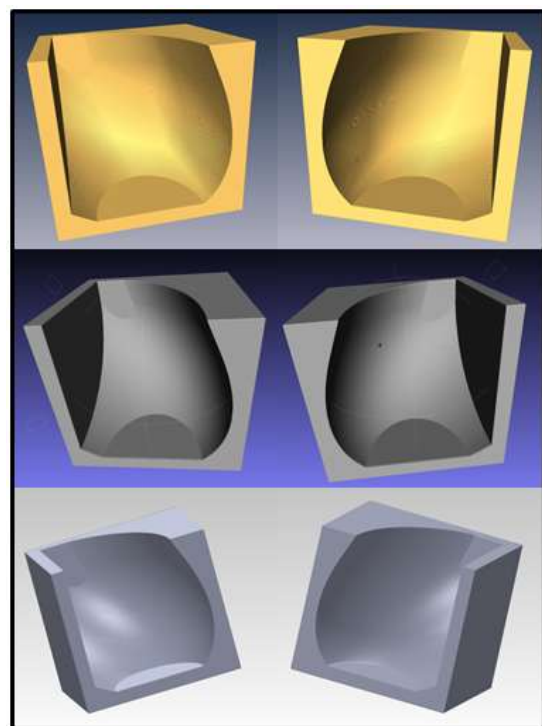


Figure 18) The breast mold rendered in Amira (top) Meshlab (middle) and Solid Works (Bottom)

More accurate tissue phantoms also were constructed. Using a model based on breast CT-scans we constructed a scalable 3-D model of a breast in IDL¹¹. We were able to highlight isolate the various structural components including ducts and lobules. The shape of these structures can therefore be either independently molded or printed with a 3-D printer. For our early work here we started-off by molding the outer shape of the breast with plans to include internal structure in future work. An image of the IDL in silico model and isolated ducts and lobular structures are depicted in figure 17. This model is scalable so that we can change the size of the molded phantoms and the correlated structure will scale proportionally.

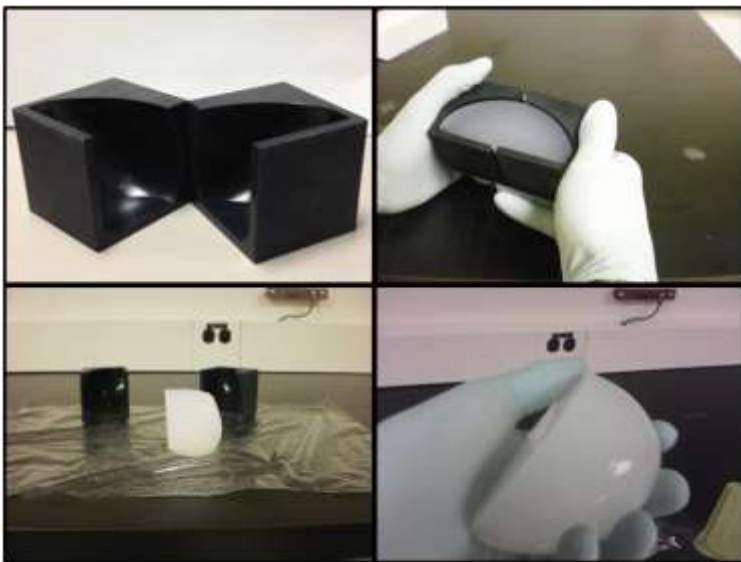


Figure 19) 3-D printed Breast phantom mold and an agar intralipid molded tissue phantom

tomography measurements of these phantoms along with the creation of inclusions representing internal structures are currently underway.

The size and shape of the breast structure was then exported from IDL into matlab to image in 2-D slices. This allowed us to generate a RAW file format that was readable by Amira as a 5x5x10cm array which was necessary to create a surface stereolithography file format (stl). The stl file was then simplified using MeshLabs, followed by Solid works. The solid works file was then 3-D printed to create the Breast phantom mold. The resulting breast phantom mold is depicted in figure 19. We have successfully molded agar Intralipid tissue phantoms using this mold. Raman

KEY RESEARCH ACCOMPLISHMENTS:

- Through Raman imaging we identified spectral markers correlated with epithelial tissue and stromal tissue.
- Through Raman imaging we demonstrated chemical contrast capable of resolving myoepithelial tissue which is an important diagnostic marker for malignant cancer.
- Contributed effort to build a stimulated Raman microscope for faster Raman imaging towards imaging larger data sets with myoepithelial tissue.
- Worked with an infrared classification model to classify 8 different tissue types present in breast tissue. This information will be used for calibrating and validating large-spot Raman acquisitions from biopsy sections.
- Improved spatial resolution achieved in Raman imaging of biopsy sections for improved tissue classification.
- Built a large-spot dark field Raman instrument for acquiring a single spectrum from a breast tissue biopsy and have collected a data set with ~80 biopsy cores.
- Built a Raman tomography instrument.
- Modified an existing Raman spectrograph to include white light illumination.
- Wrote labview software to control and automate the Raman tomography instrument.
- Collected Raman tomography data from tissue phantoms with Teflon inclusions
- Developed methods for tissue phantom fabrication and storage
- Developed a molding approach for geometrically accurate tissue phantoms

REPORTABLE OUTCOMES:

- A paper detailing the use of quantum cascade lasers to achieve infrared spectral images is included in the appendix of this report. This work investigates the use of a tunable infrared laser for imaging and is the result of efforts to improve speed and spatial resolution in the infrared imaging of breast tissue biopsies. The paper is published in the ACS Journal of Analytical Chemistry
- A paper detailing the characterization of gold nanorods with Raman report molecules in colloidal suspensions images is included in the appendix of this report. This work investigates the optimal plasmon resonance for a colloidal suspension of surfaced enhanced Raman spectroscopy nanoparticles. This is significant for our tomography work as these nanoparticles could be potential contrast agents for inclusion in phantoms or potentially as contrast agents in vivo. This paper was published in the Journal ACS Nano.
- A paper detailing that enhancement and extinction are linked and compete in a colloidal suspension of metallic nanoparticles images is included in the appendix of this report. This paper investigates the counterintuitive insight that the Raman signal vanishes when nanoparticles are excited at their plasmon resonance, while increasing nanoparticle concentrations at off-resonance excitation sometimes leads to decreased signal. This is significant for our tomography work as these nanoparticles could be potential contrast agents for inclusion in phantoms or potentially as contrast agents in vivo. This paper is published in the Journal of Physical Chemistry Letters.
- October 2012 - Oral Presentation at SciX (Formally called FACSS –Federation of Analytical Chemistry and Spectroscopy Societies)

CONCLUSION: We have made good progress towards the research described in the approved statement of work for year 2 of this research program. The results from this second year have forged a nice foundation for the work we have planned in year 3. We now have a working knowledge of some important Raman spectral bands to achieve chemical contrast between tissue types including epithelium, stroma and myoepithelium. We have a plan to collect larger data-sets with stimulated Raman imaging. We can validate the tissue-types that are present in our biopsy samples with infrared imaging through classification algorithms developed for breast tissue. Our infrared imaging capabilities now include higher spatial resolution imaging which should lead to better classification. Additionally, we built a large-spot dark field Raman instrument for acquiring a single spectrum from a breast tissue biopsy and have collected a data set with ~80 biopsy cores. We have built a Raman tomography instrument and have collected data on light scattering tissue phantoms and polymer inclusion. The tomography instrument is automated and controlled by labview code. Finally we have made good progress towards developing geometrically accurate tissue phantoms and plan to include accurate internal structures. With these accomplishments we are closer to realizing the capabilities of Raman tomography in breast tissue. We are excited to continue this work in year 3.

REFERENCES:

1. Stone, N.; Kendall, C.; Smith, J.; Crow, P.; Barr, H. Raman Spectroscopy for Identification of Epithelial Cancers. *Faraday Discuss.* **2004**, *126*, 141-157.
2. Stone, N.; Kendall, C.; Shepherd, N.; Crow, P.; Barr, H. Near-infrared Raman spectroscopy for the classification of epithelial pre-cancers and cancers. *J. Raman Spectrosc.* **2002**, *33*, 564-573.
3. Hu, M.; Yao, J.; Carroll, D.K.; Weremowicz, S.; Chen, H.; Carrasco, D.; Richardson, A.; Violette, S.; Nikolskaya, T.; Nikolsky, Y.; Bauerlein, E.L.; Hahn, W.C.; Gelman, R.S.; Allred, C.; Bissell, M.J.; Schnitt, S.; Polyak, K. Regulation of In Situ to Invasive Breast Carcinoma Transition. *Cancer Cell* **2008**, *13*, 394-406.
4. Livasy, C.A.; Karaca, G.; Nanda, R.; Tretiakova, M.S.; Olopade, O.I.; Moore, D.T.; Perou, C.M. Phenotypic evaluation of the basal-like subtype of invasive breast carcinoma. *Modern Pathology* **2006**, *19*, 264-271.
5. Barbareschi, M.; Pecciarini, L.; Cangi, M.G.; Macrì, E.; Rizzo, A.; Viale, G.; Doglioni, C. p63, a p53 homologue, is a selective nuclear marker of myoepithelial cells of the human breast. *Am. J. Surg. Pathol.* **2001**, *25*, 1054-1060.
6. Min, W.; Freudiger, C.W.; Lu, S.; Xie, X.S. Coherent nonlinear optical imaging: Beyond fluorescence microscopy. *Annual Review of Physical Chemistry* **2011**, *62*, 507-530.
7. Freudiger, C.W.; Min, W.; Saar, B.G.; Lu, S.; Holtom, G.R.; He, C.; Tsai, J.C.; Kang, J.X.; Xie, X.S. Label-free biomedical imaging with high sensitivity by stimulated raman scattering microscopy. *Science* **2008**, *322*, 1857-1861.
8. Fernandez, D.C.; Bhargava, R.; Hewitt, S.M.; Levin, I.W. Infrared spectroscopic imaging for histopathologic recognition. *Nat. Biotechnol.* **2005**, *23*, 469-474.
9. Reddy, R.K.; Walsh, M.J.; Schulmerich, M.V.; Carney, P.S.; Bhargava, R. High-definition infrared spectroscopic imaging. *Appl. Spectrosc.* **2013**, *67*, 93-105.
10. Schulmerich, M.V.; Reddy, R.; Kodali, A.K.; Elgass, L.J.; Tangella, K.; Bhargava, R. Dark field Raman microscopy. *Anal. Chem.* **2010**, *82*, 6273-6280.
11. Mahr, D.M.; Bhargava, R.; Insana, M.F. Three-dimensional in silico breast phantoms for multimodal image simulations. *IEEE Trans. Med. Imaging* **2012**, *31*, 689-697.

APPENDICES:

Paper 1: Kole, Matthew R; Reddy, Rohith K.; Schulmerich, Matthew V.; Gelber, Matthew K.; Bhargava, Rohit; Discrete Frequency Infrared Microspectroscopy and Imaging with a Tunable Quantum Cascade Laser, *Analytical Chemistry*, (2012), DOI 10.1021/ac302513f

Paper 2: Sivapalan, Seant; DeVetter, Brent M; Yang, Timothy K.; Van Dijk, Thomas; Schulmerich, Matthew V.; Carney P. Scott; Bhargava, Rohit; Murphy, Catherine J.; Off-resonance surface-enhance Raman Spectroscopy from gold nanorods suspensions as a function of aspect ratio: not what we thought, *ACS Nano* (2013), DOI 10.1021/nn305710k

Paper 3: Dijk, Thomas van; Sivapalan, Sean T.; DeVetter, Brent M.; Yang, Timothy K.; Schulmerich, Matthew V.; Murphy, Catherine J.; Bhargava, Rohit; Carney, P. Scott; Competition Between Extinction and Enhancement in Surface Enhanced Raman Spectroscopy, *J. Phys. Chem. Let.* (2013), 4(7), DOI: 10.1021/jz4005043

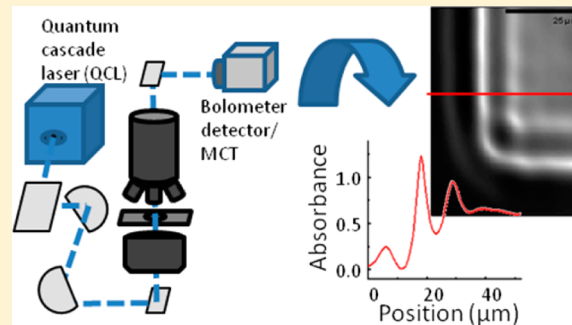
Discrete Frequency Infrared Microspectroscopy and Imaging with a Tunable Quantum Cascade Laser

Matthew R. Kole,[†] Rohith K. Reddy,[†] Matthew V. Schulmerich,[†] Matthew K. Gelber,[†] and Rohit Bhargava^{*,†,‡}

[†]Department of Bioengineering and Beckman Institute for Advanced Science and Technology, University of Illinois at Urbana–Champaign, Urbana, Illinois 61801, United States

[‡]Department of Mechanical Science and Engineering, Electrical and Computer Engineering, Micro and Nanotechnology Laboratory and University of Illinois Cancer Center, University of Illinois at Urbana–Champaign, Urbana, Illinois 61801, United States

ABSTRACT: Fourier-transform infrared (FT-IR) imaging is a well-established modality but requires the acquisition of a spectrum over a large bandwidth, even in cases where only a few spectral features may be of interest. Discrete frequency infrared (DF-IR) methods are now emerging in which a small number of measurements may provide all the analytical information needed. The DF-IR approach is enabled by the development of new sources integrating frequency selection, in particular of tunable, narrow-bandwidth sources with enough power at each wavelength to successfully make absorption measurements. Here, we describe a DF-IR imaging microscope that uses an external cavity quantum cascade laser (QCL) as a source. We present two configurations, one with an uncooled bolometer as a detector and another with a liquid nitrogen cooled mercury cadmium telluride (MCT) detector and compare their performance to a commercial FT-IR imaging instrument. We examine the consequences of the coherent properties of the beam with respect to imaging and compare these observations to simulations. Additionally, we demonstrate that the use of a tunable laser source represents a distinct advantage over broadband sources when using a small aperture (narrower than the wavelength of light) to perform high-quality point mapping. The two advances highlight the potential application areas for these emerging sources in IR microscopy and imaging.



Fourier-transform infrared (FT-IR) spectroscopy is strongly emerging for chemical mapping and imaging¹ in a variety of scientific areas^{2–6} due to technological advances since its commercial inception.⁷ FT-IR microscopic imaging⁸ is now well established for fast, spatially resolved spectroscopy,⁹ using a combination of multiplexing via rapid-scan interferometry^{10,11} and multichannel detection via array detectors. The development of multiple-element linear and faster 2D array detectors has been the principal driving force for improving widefield FT-IR microscopy via advancing hardware.³ While these detector improvements have resulted in tremendous progress, sources and spectrometer advancements have not taken place at the same rate. With notable exceptions,^{12,13} instruments use an interferometer coupled to a thermal source. Setups based on thermal sources are exceptionally efficient, stable, and commercially successful; however, practitioners have to acquire a large bandwidth of data even if they are interested in only a small set of wavelengths. A smaller set has been shown to be particularly useful, for example, in tissue classification¹⁴ or for monitoring dynamic processes in polymers.¹⁵ Techniques which save time by probing only bands of interest may facilitate rapid data acquisition and analyses. As opposed to FT-IR spectroscopic methods, hence, measurements of a few, selected spectral features may be desirable in some areas.

Approaches to accomplish the same may be termed discrete frequency IR (DF-IR) spectroscopy methods.¹ One straightforward approach to DF-IR spectroscopy and imaging is to use a grating. The use of a dispersive or scanning monochromator for IR microscopy is uncommon due to the inherent low blackbody illumination intensity at individual wavelengths, thereby forfeiting Jacquinot's advantage as well as the spectral multiplexing (Fellgett) advantage.¹⁶ In imaging, the multiplexing advantage may be recovered somewhat by using an array detector, but a configuration in which part of the array is used for spectral and part for spatial measurements compromises the imaging potential. While sources such as a synchrotron can potentially provide the flux to overcome the throughput disadvantage,^{17,18} a recent emphasis in the use of synchrotrons has instead been to use the brightness of the source to perform high-resolution imaging,¹⁹ which would not provide sufficient flux for nonmultiplexed methods. Narrow-band filters may enable both widefield imaging and DF-IR spectroscopy but are only now maturing as a technology and are intensity limited by the coupled broadband source.²⁰

Received: August 31, 2012

Accepted: October 31, 2012

Published: October 31, 2012



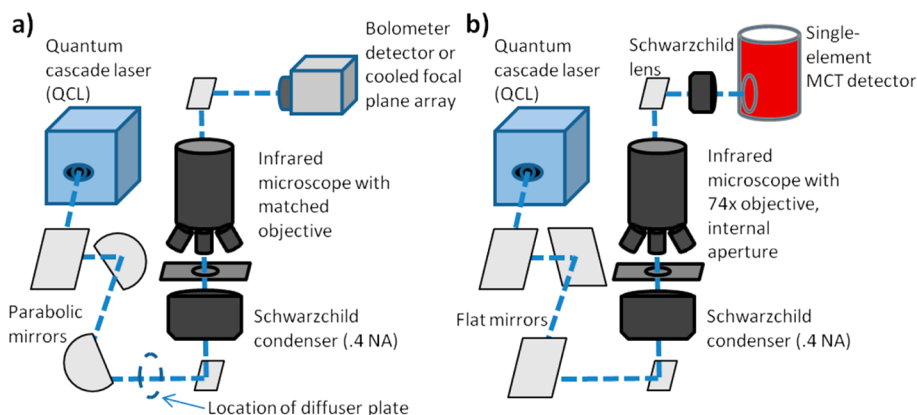


Figure 1. Schematics of the two DF-IR systems evaluated in these experiments. Both utilize a tunable, narrow-bandwidth mid-infrared QCL and the same infrared microscope frame. (a) QCL coupled to an uncooled bolometer camera. A parabolic mirror pair is used for 10:1 beam expansion before the microscope. For one experiment, a cooled focal plane array (FPA) was substituted for the bolometer. (b) A cooled single-element MCT detector is utilized with an adjustable aperture that focuses at the sample plane for point measurements. Flat mirrors replace the parabolic mirror pair so that the beam is not expanded.

Recently, narrow-bandwidth quantum cascade lasers (QCLs) have become available. In their most common implementation, QCLs are tunable, external-cavity mid-infrared lasers with outputs on the order of hundreds of milliwatts and grating-assisted spectral selection. First developed in the 90's,²¹ these devices have been previously used in the detection of trace particles in gases,²² wavelength-modulation absorption measurements,²³ and in photoacoustic spectroscopy.²⁴ Early QCLs featured too limited a spectral range to be useful for general spectroscopic analyses. While the tunable range of individual QCLs still covers only a small region of the mid-IR spectrum (for example, here we use a QCL over the range 980–1204 cm⁻¹), these devices represent emerging sources with broad tunable ranges, high power, and narrow bandwidths which are suitable for mid-IR spectroscopy. Additionally, these characteristics may render these new lasers suitable as sources for discrete frequency infrared spectroscopy or microscopy. The use of QCLs for IR imaging has been proposed and demonstrated^{25–27} but not in a microscopy format. It is presently unclear whether QCLs offer a microscopy advantage over FT-IR imaging and what specific advances may be enabled by the higher flux. In this manuscript, we describe the use of a QCL as a source in microscopic imaging and point-mapping. By coupling the bright source to an infrared microscope, we take advantage of the laser's high power to perform imaging in a DF mode and compare the results to FT-IR imaging. We also examine whether a low-cost bolometer can be used as a widefield detector alternative to the current standard of expensive liquid nitrogen-cooled detectors. Further extending attainable data quality, we examine the possibility for high-resolution point mapping based on recent theory²⁸ using a micrometer-sized aperture. As QCLs are a coherent source, finally, we describe the implications of spatial coherence with regards to imaging.

EXPERIMENTAL SECTION

Instrumentation. The instrumentation, set up in-house, consists of three main components: a narrow bandwidth (<1 cm⁻¹ spectral bandwidth over the tunable range of 980–1204 cm⁻¹) quantum cascade laser (Daylight Solutions, San Diego, CA, prototype of model UT-9), an infrared microscope (Varian Inc., Palo Alto, CA), and detectors. Two detectors were used: a

microbolometer camera with a 324 × 256 pixel detector (Photon series, FLIR, Boston, MA) and a liquid nitrogen-cooled single element mercury cadmium telluride (MCT) detector (InfraRed Associates, Stuart, FL), and in a second widefield imaging configuration, we employed a cooled focal plane array (FPA) in place of the bolometer (Santa Barbara Focal Plane, Santa Barbara, CA). For widefield imaging, the output beam from the QCL was expanded 10:1 (from a 6 mm beam diameter to approximately 60 mm) via two gold-coated parabolic mirrors. The expanded beam was passed through an iris and entered the side port of the infrared microscope. In transmission mode, the beam was condensed through a 0.5 NA Schwarzschild objective lens before passing through the sample stage. The beam exiting the sample stage was collected using a matched 15× Schwarzschild reflecting objective. The image was then passed through the microscope's open aperture and imaged onto the bolometer. For point-mapping measurements, the same configuration was used, but apertures of variable openings were placed in the beam path after the sample to restrict light to be from a defined spatial region of the sample. Beam expansion optics were removed, and the single element detector was also used in place of the array detector.

A rotating diffuser plate consisting of a one inch diameter, scratched calcium fluoride plate, and a small motor was employed in certain portions of the experiment to reduce coherence effects. When in use, it was placed between the second parabolic mirror and the iris, after beam expansion but before the microscope entrance. With the rotating diffuser in place, 64 sequential frames were acquired for each wavelength. These were averaged in order to correct for the changing position of the plate. Acquiring a series of individual frames was necessary because the limited dynamic range of the bolometer prevented integration times from being equal to one period of the diffuser rotation. Single frames were acquired for images without the diffuser. While obviously affecting the signal-to-noise ratio of the data, we do not consider this aspect here as our aim was to obtain imaging contrast.

A commercial FT-IR imaging spectrometer (Spotlight 400, Perkin-Elmer, Waltham, MA) was also used as a performance standard to compare with the instrument described above. The spectrometer was operated in rapid scan mode at a mirror speed of 1 cm/s. Data were acquired and truncated to the 4000–720 cm⁻¹ range of interest. N–B medium apodization

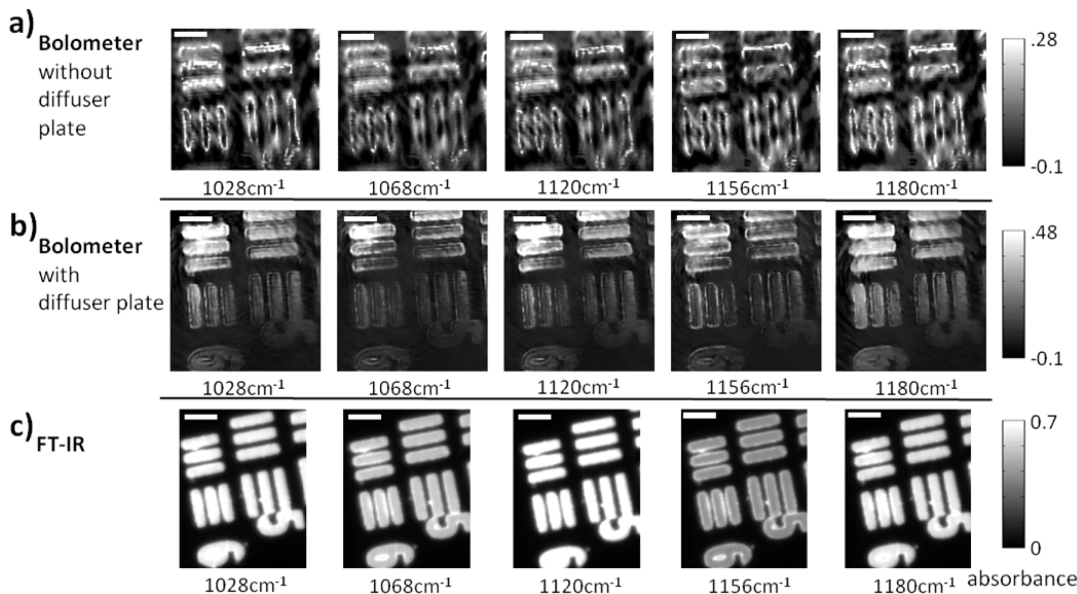


Figure 2. USAF 1951 optical resolution target absorption images (cycle 3, elements 5 and 6) as acquired by three different instruments. (a) QCL + bolometer system without diffuser plate. (b) QCL + bolometer system with rotating diffuser plate. (c) Commercial FT-IR instrument. Please note the differences in the color bars between the three sets of images. The scale bar in the images denotes 100 μm .

was used for spectral transformation, and a suitable background was acquired from a region adjacent to the sample.

Data Acquisition and Processing. The test sample in this manuscript was a USAF 1951 optical resolution (bar) target fabricated in-house. Briefly, during the fabrication process, uncured SU-8 photoresist resin was spin-coated onto a barium fluoride substrate to a desired thickness, cured, postbaked, and solvent-developed. The target is evaluated using optical microscopy to confirm geometric fidelity. Elements 5 and 6 of cycle 3 were imaged in all instances. All image processing was performed in ENVI (ITT Visual Information Solutions, Boulder, CO) and Matlab (The MathWorks, Nantucket, MA) using code written in-house. Single-beam images had no correction applied, while absorbance images had been divided by a reference image consisting of an unmodified barium fluoride substrate. Images taken at discrete frequencies with the QCL and the bolometer also have a “dark current” chip image subtracted from both the single-beam and background images.

Safety Considerations. The quantum cascade laser is the single most hazardous component of the experiments outlined in this manuscript. Depending on the operating wavelength, the output can exceed 400 mW. As a well-collimated beam with a diameter of ~6 mm, the maximum permissible exposure (MPE) of this radiation is reached in less than one second as defined by ANSI Z136.1.²⁹ Additionally, all output frequencies are invisible to the eye, adding to the potential risk of exposure. Lab personnel operating these devices should be trained in laser safety and wear high optical density (OD7+) eye protection at all times.

RESULTS AND DISCUSSION

Optical microspectroscopy and imaging configurations to conduct experiments described in this manuscript were set up. A schematic of the two major setups is shown in Figure 1. These flexible configurations allowed us to perform a number of experiments by changing aspects of the optical train, as needed, to understand the different effects associated with using QCLs. For this preliminary study, we chose to image a USAF

1951 optical resolution bar target, which has historically been used as a standard for measuring the performance of imaging instrumentation. The target features a motif of three equally spaced rectangles which is patterned many times in decreasing sizes. The particular target used in this manuscript consisted of an approximately 10 μm thick layer of an SU-8 polymer (which has a distinctive IR absorption spectrum) on a barium fluoride substrate (which is transparent to mid-infrared light). In all examples, we examined one region of the target: cycle 3, elements 5 and 6, which contain “bars” of widths approximately 39 and 35 μm , respectively. This particular structure was chosen because it approaches the size limit for targets which are well-resolved by commercial FT-IR imaging instruments.

We first acquired images of the standard USAF sample using a bolometer array detector, shown in Figure 2a. Uncooled detectors have also been proposed for use in IR spectroscopic-imaging measurements, but coupling a bolometer to a globar source produced exceptionally low signal-to-noise data.³⁰ The higher flux of the QCL (hundreds of milliwatts with a spectral width $<1 \text{ cm}^{-1}$ versus tens of microwatts from wavelength 5–10 μm for a typical globar source³¹) makes imaging with a microbolometer feasible. The lower cost of the microbolometer, as well as its larger format compared to the majority of cooled array detectors available, makes this a very attractive technology. With a more even illumination, such an imaging system could compete against the established FT-IR imaging systems that usually employ a thermal source (globar) and a cooled array detector. The data acquired using a QCL were compared to those acquired from a commercial FT-IR imaging spectrometer in Figure 2c. It is notable that the QCL-based system used a low-performance bolometer, while the FT-IR imaging system is the best available today in terms of signal-to-noise ratio (SNR). The data demonstrate that the coupling of a QCL to an imaging system can be achieved and presents an opportunity to compare with FT-IR imaging systems, even though the two sources are significantly different in nature.

A fine structure overlain with the target was apparent in the QCL-based data and was the most striking difference from the

FT-IR imaging data. We hypothesized that this effect arose from multiple reflections and scattering from the sample as well as etaloning, both of which were exacerbated by the spatial coherence of the laser. To alleviate this problem, we placed a diffusing element in the beam path. With the use of this diffuser (Figure 2b), the fringes and interference were not entirely eliminated but image quality was substantially improved. Such a diffuser has been used in at least one other study,³² but its effect was not presented, and the effects of laser coherence on images were not shown. The diffuser employed was a transparent salt plate that was heavily scratched on one face to induce random phase shifts in the beam. Simply placing the plate in the path of the beam had little effect, as a structure to the spatial correlation in the beam was still transmitted (images not shown). As a result, the diffuser plate was rotated. Rotating the plate allows energy to be evenly distributed over the specimen, but a drawback is that multiple images have to be acquired in order to average out rotation artifacts. Images acquired by the QCL/bolometer instrument with the diffuser plate can be seen in Figure 2b. Compared to Figure 2a, the fine structure is markedly reduced. A slight shadowing effect can be seen in both sets of images, partly the result of an imperfectly aligned system and the presence of a central obscuration in all Schwarzschild objectives. Even with rotation, the collected image is a function of the exact rotational position of the plate at the time of acquisition. Scratching the plate cannot yield completely randomized scattered light in general; consequently, regions of pronounced scratches or less scratching retain some coherence and are projected through the sample and onto the bolometer. A series of 64 sequential images was captured and averaged to “smooth out” this enduring structure. As it is not a perfect solution, the “swirling” pattern caused by the rotating diffuser plate is evident in the images, but this degrades the images far less than without the diffuser in place. In addition to reducing the coherence of light, the scratched diffuser plate also causes additional scattering. This is ordinarily undesirable, as light scattered (or absorbed) by the plate cannot be used for imaging, but in this setup the losses were small compared to the available flux.

The effects of the beam’s spatial coherence are clearly an issue of concern if QCLs are to be used for IR imaging. A theoretical framework to explain image formation including the light coherence is desirable. Using coherent light, every detector element (P') has electric field contribution, not only from the corresponding point (P) on the sample being imaged but also from every other point around P within a radius determined by the coherence area.³³ If the source is coherent, photons incident at different spatial locations of the sample are in phase with one another. The electric field associated with light scattered at any point from the sample can interfere with light transmitted from other points. The amplitude of the interfered electric fields are added and quadratically encoded in the resulting intensity, which is measured by the detector. Hence, the detector image is the result of both the corresponding image that would be observed using an incoherent source as well as the effects of spatial interference. A complete description of the recorded absorbance is possible using recently developed electromagnetic theory-based models of image formation in IR microscopes and specific sample shapes.^{34–36} Here, we extend a more recent formulation that is especially useful for examining the effects on recorded data of periodic structures in the samples.³⁷ For the purposes of simulation in this study, we modified the previously reported

framework to include beam coherence, and the resulting scattered and transmitted fields were added. To improve image quality and more accurately document the effects of coherence, the bolometer was temporarily replaced with a cooled FPA. The results are shown in Figure 3.

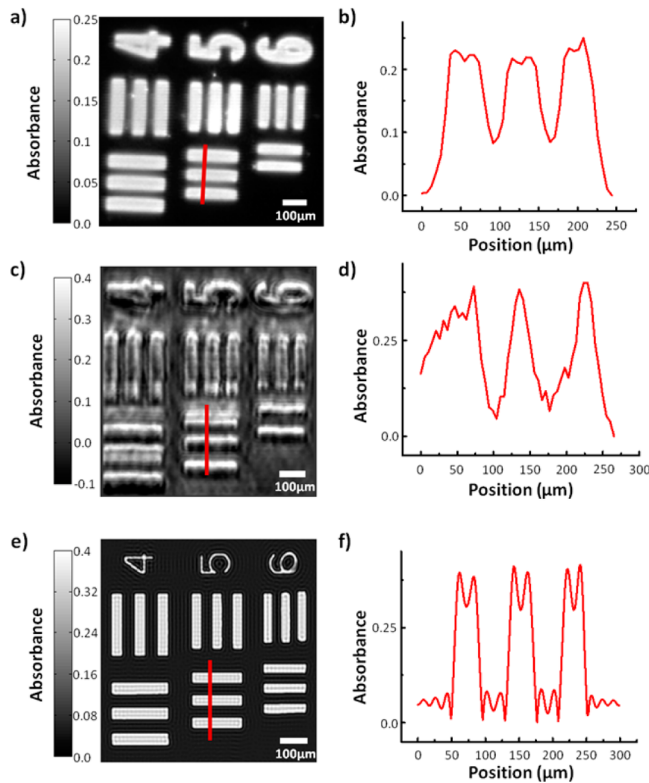


Figure 3. (a) Commercial (globar source) infrared absorbance image of a USAF 1951 optical resolution target (cycle 3, elements 4 through 6) at 1180 cm^{-1} . (b) A profile of three bars of element 5, indicated by the red line in (a). (c) QCL + FPA absorbance image of the same target at 1180 cm^{-1} . Note that there is no longer a diffuser plate in the beam path such that full coherent effects are present. (d) A profile of three bars of element 5, indicated by the red line in (c). (e) Simulated absorbance image of the same region at 1180 cm^{-1} assuming a coherent source. (f) A profile of three simulated bars of element 5, indicated by the red line in (e).

The simulations indicate that the effects of coherence are to impart a fine structure in the recorded absorbance. The most striking feature of the source can be seen in the extracted absorbance profiles at an edge. While data from the globar-equipped system showed an apparent absorbance increase at the edge due to scattering,³⁸ the fine structure of the beam extends considerably beyond the edge in the QCL-based system. Although this observation and modeling of the fine structure serves as a caution to the use of QCLs and interpretation of recorded data, it also presents new opportunities in modeling and, perhaps, extracting additional information about the structure of the sample. At this time, however, the expectation that the only outcome of a simple coupling of QCLs to existing microscopy systems would be to obtain an equivalent system but with higher SNR is unfounded. The fringes in the recorded images contain information about sample structure which can be extracted via careful theory, modeling, and signal processing. While the formulation of these reconstructions is beyond the scope of this manuscript, a

practical concern is that the signal-to-noise ratio needs to be high for the reconstruction to be reliable. Comparison of theoretical and experimental data demonstrate that further optimization of the optical setup and experimental parameters is required.

In comparing bolometer measurements to those acquired by a commercial FT-IR system, “image quality” can be described by several different factors, including spatial resolution, spectral quality, and signal-to-noise ratio. The spatial resolution of a system is defined completely by wavelength, numerical aperture, and effective detector pixel size. While the QCL instrument utilizes a smaller numerical aperture objective, it can be observed from the measured profiles that resolution does not appear to differ wildly between the two, as is expected. Figure 4a shows the bar motif profiles for target S, cycle 3 for

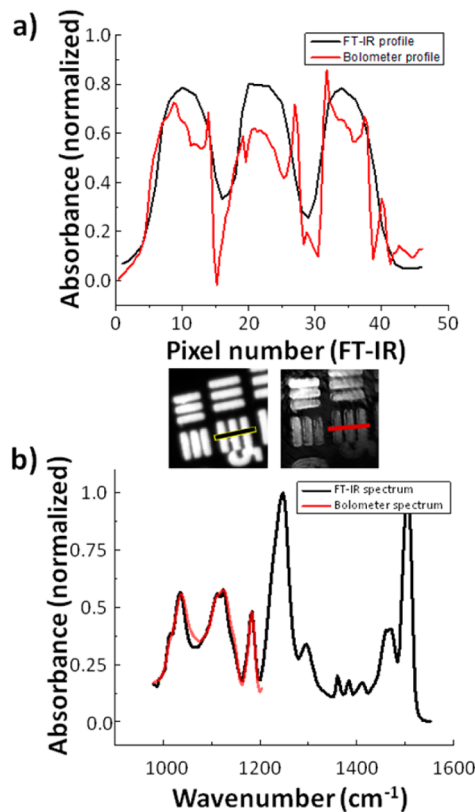


Figure 4. (a) Bar-target profile for a commercial FT-IR instrument and the QCL + bolometer system as indicated by the black and red line segments. Because the two detectors contain a different number of pixels, the scale of the measured bolometer profile was adjusted to match that of the commercial instrument. (b) Overlaid absorption spectra of the SU-8 polymer for both the commercial FT-IR system and the QCL + bolometer system. The commercial system recovers the spectrum using an inverse Fourier transform recorded by an interferometer with a 0.25 cm maximum retardation ($\sim 4 \text{ cm}^{-1}$ resolution). The discrete absorbance measurements were taken every 4 cm^{-1} for the bolometer system by tuning the QCL sequentially.

both the commercial FT-IR instrument and the bolometer plus diffuser plate setup. After a correction for pixel size (the size per pixel in the FT-IR images is almost 2.5 times as large as those in the bolometer images), it is apparent that the two are on the same order. As there are more pixels representing the same area for the bolometer images, this system has the potential to achieve higher quality images. The relative equivalence of

images is not surprising as the optical setup is similar; however, the relative equivalence in the presence of coherence effects is encouraging. This may indicate that QCL-based systems could be effective for qualitative imaging and will reasonably correlate with FT-IR imaging data, provided that absorbance is high and scattering is not especially strong. For weak absorbance and domain sizes on the order of the wavelength, results between the two would deviate significantly.

Arguably more important than the resolution in chemical imaging is the quality of the recorded spectra. When sequential images across a range of evenly spaced wavelengths are acquired, an absorption spectrum at each pixel is generated. Figure 4b shows the spectrum of SU-8 as acquired by the bolometer instrument with a diffuser plate and as acquired by the commercial FT-IR system. It is clear from the similarity of the band shapes that the bolometer instrument is capable of collecting a representative spectrum. While the band intensities are not identical to those determined by the commercial instrument, this is to be expected. Bolometers are inherently noisier than cooled focal plane arrays and are generally not considered capable of quantitative measurements. While not explicitly observed, it is probable that these power fluctuations can be exacerbated at the far limits of the laser’s tunable range. The differences may also be due to optical effects, as reported previously for other configurations,^{34–38} but need to be examined in detail using available theory and simulations. The SNR of acquired data is another important aspect of image quality which should be evaluated. Due to uneven illumination in this unoptimized setup, we have measured the signal-to-noise ratio as varying from less than 1 to as large as 32. These values are for images whose acquisition time is on the order of milliseconds and signal averaging may well-improve the SNR if the noise is detector dominated. It can be argued that the QCL system has a higher capacity for signal-to-noise ratio than does the FT-IR instrument: not only is the source power much higher at each individual wavelength measured (between 200 mW and 400 mW at most wavelengths), but the entire dynamic range of the detector is used for a single wavelength at a time rather than evaluating all wavelengths simultaneously. Finally, the QCL-bolometer system underperforms the commercial FT-IR imaging system, indicating the need for further improvement. When these challenges are addressed, the QCL-bolometer system will offer advantages over FT-IR imaging for certain applications. The higher flux makes measurement in aqueous environments possible.³⁹ Only a handful of bands are required for certain biological analyses,¹⁴ making acquisition of the entire spectrum redundant. Discrete frequency methods could offer a distinct speed advantage in cases where only some bands are required for measurement. Additionally, due to the direct acquisition of data without the need for performing a Fourier transform, the possibility for real-time infrared microscopy and monitoring becomes available.

Given the multichannel detection advantage and the emergence of IR imaging systems with exceptional quality,^{2,19} we focused on widefield microscopy applications of the QCL source. Interferometric instrumentation is not appropriate for point-mapping applications due to the very low throughput of a broadband source through a small aperture. In comparison, a potential use for QCLs as IR spectroscopy sources may lie in high-throughput point-mapping measurements. The large flux, focused into a single channel, may offset some of the speed advantages of multichannel detection and the need to diffuse the beam over a large area. The use of point illumination may

also be used to circumvent the fine structure seen in images, as there would not be a scattered and transmitted wave at two different points to interfere. As a final instrumentation setup, we examined the use of QCL for point mapping.⁹ For point mapping, the expansion optics (gold-coated parabolic mirrors, iris) and diffuser plate were removed from the DF-IR setup. This kept the unaltered beam tightly focused (less than 2 mm diameter) upon entering the microscope. The bolometer camera was replaced with a cooled single-element MCT detector, allowing for enhanced sensitivity. For simple point measurements by rastering large areas, a QCL system will not be able to best an FT-IR imaging system with a globar source. The speed of these conventional widefield systems would far outperform QCL point mapping; the advantage of a QCL source lies in the ability to create truly diffraction-limited spot sizes with large NA objectives and small apertures. We replaced our objective with a 74 \times Schwarzschild objective of 0.65 NA. The high magnification of the objective meant that the microscope's built-in adjustable square aperture could be used to create a very small effective aperture (0.72 μm) for point-imaging. This aperture size is significantly smaller than the range of illumination wavelengths for imaging and smaller than any objective reported for a globar or synchrotron-based system.^{40–42} Even with this small aperture in place, a large SNR was observed, and by rastering the stage in increments of 1 or 0.5 μm , spectral data were obtained over larger areas. To date, this is the smallest far-field aperture and smallest point spacing reported. While we caution that diffraction still limits the spot size and therefore the resolution that can be achieved, the image improvement over the use of $\sim 10 \mu\text{m}$ apertures is obvious in the recorded data. Figure 5 demonstrates data

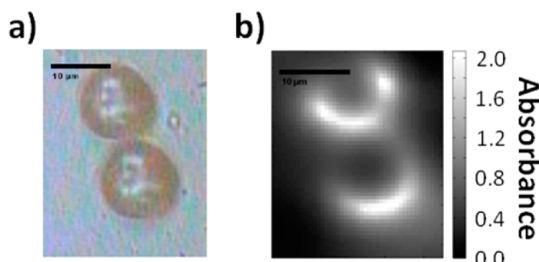


Figure 5. (a) White-light image of two touching polystyrene spheres, diameter 10 μm . (b) Point-mapping IR absorption image of the same two spheres at 1080 cm^{-1} , 0.5 μm steps, 0.72 μm aperture.

acquired from two polystyrene spheres that are approximately 10 μm in diameter. The pixel density is over 100 times that of a synchrotron and nearly 1000 times more than that of a globar.¹⁹ For localizing samples in a microscopy configuration, QCL-based point-mapping systems present a new opportunity to image small regions and generate images that are of high pixel density for small feature recognition. The reproduction of structure is quite faithful. At $\sim 10 \mu\text{m}$ of imaging wavelength, the 10 μm diameter spheres can be clearly seen and easily separated.

This point-mapping method also allows for the investigation of scattering effects with enhanced clarity. Scattering by the edges of structural features in infrared imaging is extensive but difficult to quantify in a widefield regime. The corner of one of the bars in the USAF 1951 optical resolution target from the first set of experiments was imaged with both a commercial FT-IR instrument and the point-mapping setup to compare the

clarity of scattering effects. As imaged by the commercial system in Figure 6a, the feature shows an increased loss of

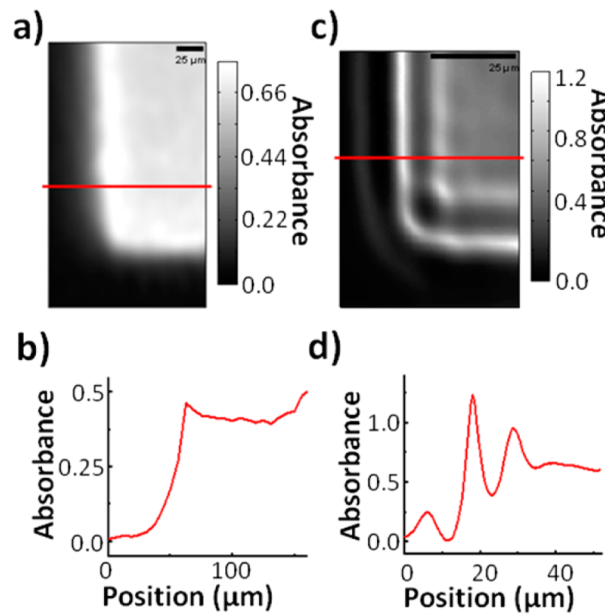


Figure 6. (a) Image of a USAF 1951 bar target corner with a commercial FT-IR instrument. The increased "absorbances" at the sharp feature edges are actually due to increased scattering. (b) Graphical profile of one row of pixels from (a). Aside from some blurring, there does not appear to be a well-defined interference pattern at the feature edges due to scattering. (c) Image of the corner with the point-mapping instrument and a 0.72 μm aperture. The edge structure looks starkly different from that of (a). (d) Graphical profile of one row of pixels from (c). Each edge shows a series of minima and maxima that were not discernible with a commercial FT-IR instrument.

transmission at the edges (misinterpreted by the instrument as increased absorbance). The image shows no well-defined structure to the increased scattering. This is evidenced by Figure 6b which shows an absorbance profile of one row of pixels in the image. When imaged by the point-mapping QCL system in 0.5 μm steps, it becomes apparent that there is a well-defined structure to the scattering that was not discernible in the globar image. Figure 6c shows the multiple spatial maxima and minima that occur with edge scattering, and Figure 6d shows one row of pixels in greater detail. The richness of information from the edge deserves increased examination and is likely to spur further interest in understanding image formation in the IR.

CONCLUSION

The latest developments in tunable QCL technology have large tuning ranges, narrow spectral linewidths, and high fluxes to the point where these become feasible sources for discrete-frequency infrared imaging. We have demonstrated an application of a QCL for use as a source in infrared microscopy. When coherence is reduced and the beam is expanded, images of an optical resolution target can be acquired on a bolometer-type camera. These images are comparable to commercial FT-IR measurements in spatial resolution but lack in spectral clarity and signal-to-noise ratio. When used for point mapping, the QCL provides a throughput advantage unmatched by incoherent broadband sources and allows for high-resolution

infrared imaging through a small aperture. These properties of QCLs as an infrared source allow for additional advantages, including rapid widefield imaging at single wavelengths, enhanced localization of signal, and the possibility for real-time infrared monitoring.

AUTHOR INFORMATION

Corresponding Author

*E-mail: rxb@illinois.edu. Address: 4265 Beckman Institute, University of Illinois at Urbana–Champaign, 405 N. Mathews Avenue, Urbana, IL 61801. Tel: (217) 265-6596.

Notes

The authors declare no competing financial interest.

ACKNOWLEDGMENTS

The described work was supported by the National Science Foundation (CHE 0957849) and the National Institutes of Health (R01EB009745). M.V.S. would like to acknowledge support through the Congressionally Directed Medical Research Program Postdoctoral Fellowship (BC101112).

REFERENCES

- (1) Bhargava, R. *Appl. Spectrosc.* **2012**, *66* (10), 1091–1120.
- (2) Walsh, M. J.; Reddy, R. K.; Bhargava, R. *IEEE J. Sel. Top. Quantum Electron.* **2012**, *18* (4), 1502–1513.
- (3) Levin, I. W.; Bhargava, R. *Annu. Rev. Phys. Chem.* **2005**, *56*, 429–474.
- (4) Bhargava, R.; Wang, S. Q.; Koenig, J. L. *Adv. Polym. Sci.* **2003**, *163*, 137–191.
- (5) Prati, S.; Joseph, E.; Sciuotto, G.; Mazzeo, R. *Acc. Chem. Res.* **2010**, *43* (6), 792–801.
- (6) Bellisola, G.; Sorio, M. *Am. J. Cancer Res.* **2012**, *2*, 1–21.
- (7) Kwiatkoski, J. M.; Reffner, J. A. *Nature* **1987**, *328* (27), 837–838.
- (8) Lewis, E. N.; Treado, P. J.; Reeder, R. C.; Story, G. M.; Dowrey, A. E.; Marcott, C.; Levin, I. W. *Anal. Chem.* **1995**, *67* (19), 3377–3381.
- (9) Bhargava, R.; Wall, B. G.; Koenig, J. L. *Appl. Spectrosc.* **2000**, *54* (4), 470–479.
- (10) Huffman, S. W.; Bhargava, R.; Levin, I. W. *Appl. Spectrosc.* **2002**, *56* (8), 965–969.
- (11) Snively, C. M.; Katzenberger, S.; Oskarsdottier, G.; Lauterbach, J. *Opt. Lett.* **1999**, *24* (24), 1841–1843.
- (12) Elmore, D. L.; Tsao, M. W.; Frisk, S.; Chase, D. B.; Rabolt, J. F. *Appl. Spectrosc.* **2002**, *56* (2), 145–149.
- (13) Liu, J. N.; Schulmerich, M. V.; Bhargava, R.; Cunningham, B. T. *Opt. Express* **2011**, *19* (24), 24182–24197.
- (14) Bhargava, R. *Anal. Bioanal. Chem.* **2007**, *389* (4), 1155–1169.
- (15) Lendl, B.; Schindler, R. *Vib. Spectrosc.* **1999**, *19* (1), 1–10.
- (16) Griffiths, P. R.; De Haseth, J. A. *Fourier Transform Infrared Spectrometry*, 2nd ed.; John Wiley & Sons: Hoboken, NJ, 2007.
- (17) Hirschmugl, C. J.; Gough, K. M. *Appl. Spectrosc.* **2012**, *66* (5), 475–491.
- (18) Petibois, C.; Piccinini, M.; Guidi, M. C.; Marcelli, A. J. *Synchrotron Radiat.* **2010**, *17* (1), 1–11.
- (19) Nasse, M. J.; Walsh, M. J.; Mattson, E. C.; Reininger, R.; Kajdacsy-Balla, A.; Macias, V.; Bhargava, R.; Hirschmugl, C. J. *Nat. Methods* **2011**, *8*, 413–416.
- (20) Kodali, A. K.; Schulmerich, M.; Ip, J.; Yen, G.; Cunningham, B. T.; Bhargava, R. *Anal. Chem.* **2010**, *82* (13), 5697–5706.
- (21) Faist, J.; Capasso, F.; Sivco, D. L.; Sirtori, C.; Hutchinson, A. L.; Cho, A. Y. *Science* **1994**, *264* (5158), 553–556.
- (22) Kosterev, A. A.; Tittel, F. K. *IEEE J. Quantum Electron.* **2002**, *38* (6), 582–591.
- (23) Namjou, K.; Cai, S.; Whittaker, E. A.; Faist, J.; Gmachl, C.; Capasso, F.; Sivco, D. L.; Cho, A. Y. *Opt. Lett.* **1998**, *23* (3), 219–223.
- (24) Paldus, B. A.; Spence, T. G.; Zare, R. N.; Oomens, J.; Harren, F. J. M.; Parker, D. H.; Gmachl, C.; Cappasso, F.; Sivco, D. L.; Baillargeon, J. N.; Hutchinson, A. L.; Cho, A. Y. *Opt. Lett.* **1999**, *24* (3), 178–180.
- (25) Weida, M. J.; Buerki, P. R.; Pushkarsky, M.; Day, T. *Micro- and Nanotechnology Sensors, Systems, and Applications* **2011**, *8031*, 803127.
- (26) Brandstetter, M.; Genner, A.; Anic, K.; Lendl, B. *Procedia Eng.* **2010**, *5*, 1001–1004.
- (27) Phillips, M. C.; Ho, N. *Opt. Express* **2008**, *16* (3), 1836–1845.
- (28) Reddy, R.; Davis, B.; Carney, P. S.; Bhargava, R. *IEEE I. S. Biomed. Imaging* **2011**, 738–741.
- (29) American National Standard for Safe Use of Lasers; ANSI Z136.1; Laser Institute of America: Orlando, 2007.
- (30) Haka, A. S.; Levin, I. W.; Lewis, E. N. *Appl. Spectrosc.* **2000**, *54* (5), 753–755.
- (31) Kwon, B.; Schulmerich, M. V.; Elgass, L. J.; Kong, R.; Holton, S. E.; Bhargava, R.; King, W. P. *Ultramicroscopy* **2012**, *116*, 56–61.
- (32) Amrani, H.; McCrow, A.; Phillips, C. *Rev. Sci. Instrum.* **2009**, *80*, 123702.
- (33) *Principles of Optics: Electromagnetic Theory of Propagation, Interference and Diffraction of Light*, 6th ed.; Born, M., Wolf, E., Eds.; Cambridge University Press: Cambridge, United Kingdom, 2006.
- (34) Davis, B. J.; Carney, P. S.; Bhargava, R. *Anal. Chem.* **2010**, *82*, 3487–3499.
- (35) Davis, B. J.; Carney, P. S.; Bhargava, R. *Anal. Chem.* **2010**, *82*, 3474–3486.
- (36) Davis, B. J.; Carney, P. S.; Bhargava, R. *Anal. Chem.* **2011**, *83*, 525–532.
- (37) Reddy, R. K.; Walsh, M. J.; Schulmerich, M. V.; Carney, P. S.; Bhargava, R. *Appl. Spectrosc.* **2012**, In press.
- (38) Bhargava, R.; Wang, S. Q.; Koenig, J. L. *Appl. Spectrosc.* **1998**, *52*, 323–328.
- (39) Schaden, S.; Haberkorn, M.; Frank, J.; Baena, J. R.; Lendl, B. *Appl. Spectrosc.* **2004**, *58* (6), 667–670.
- (40) Dumas, P.; Carr, G. L.; Williams, G. P. *Analisis* **2000**, *28* (1), 68–74.
- (41) Jamin, N.; Dumas, P.; Moncuit, J.; Fridman, W.-H.; Teillaud, J.-L.; Carr, G. L.; Williams, G. P. *Proc. Nat. Acad. Sci. U.S.A.* **1998**, *95* (9), 4837–4840.
- (42) Miller, L. M.; Smith, R. J. *Vib. Spectrosc.* **2005**, *38* (1–2), 237–240.

Off-Resonance Surface-Enhanced Raman Spectroscopy from Gold Nanorod Suspensions as a Function of Aspect Ratio: Not What We Thought

Sean T. Sivapalan,[†] Brent M. DeVetter,^{‡,§} Timothy K. Yang,[⊥] Thomas van Dijk,^{||} Matthew V. Schulmerich,^{§,||} P. Scott Carney,^{‡,§} Rohit Bhargava,^{‡,§,||,¶,*} and Catherine J. Murphy^{†,⊥,*}

[†]Department of Materials Science and Engineering, [‡]Department of Electrical and Computer Engineering, [§]Beckman Institute for Advanced Science and Technology, [⊥]Department of Chemistry, ^{||}Department of Bioengineering, and [¶]Department of Mechanical Science and Engineering, Micro and Nanotechnology Laboratory and University of Illinois Cancer Center, University of Illinois at Urbana—Champaign, Urbana, Illinois 61801, United States

ABSTRACT Design of nanoparticles for surface-enhanced Raman scattering (SERS) within suspensions is more involved than simply maximizing the local field enhancement. The enhancement at the nanoparticle surface and the extinction of both the incident and scattered light during propagation act in concert to determine the observed signal intensity. Here we explore these critical aspects of signal generation and propagation through experiment and theory. We synthesized gold nanorods of six different aspect ratios in order to obtain longitudinal surface plasmon resonances that incrementally spanned 600–800 nm. The Raman reporter molecule methylene blue was trap-coated near the surface of each nanorod sample, generating SERS spectra, which were used to compare Raman signals. The average number of reporter molecules per nanorod was quantified against known standards using electrospray ionization liquid chromatography mass spectrometry. The magnitude of the observed Raman signal is reported for each aspect ratio along with the attenuation due to extinction in suspension. The highest Raman signal was obtained from the nanorod suspension with a plasmon resonance blue-shifted from the laser excitation wavelength. This finding is in contrast to SERS measurements obtained from molecules dried onto the surface of roughened or patterned metal substrates where the maximum observed signal is near or red-shifted from the laser excitation wavelength. We explain these results as a competition between SERS enhancement and extinction, at the excitation and scattered wavelengths, on propagation through the sample.



KEYWORDS: surface-enhanced Raman spectroscopy · extinction · gold nanorods

Surface-enhanced Raman scattering (SERS) is a vibrational technique whose promise for chemical sensing has been debated since the 1970s.¹ A primary design objective in SERS optimization is to tailor the surface plasmon resonance relative to the laser excitation wavelength. This is because the on-resonance field enhancement at the surface of the plasmon-active material can increase the Raman signal intensity of nearby molecules by several orders of magnitude. In the case of SERS on immobilized silver nanostructures, the maximum signal enhancement was observed if the plasmon band position was red-shifted compared to the laser excitation wavelength.² On the basis of these studies, researchers have

fabricated rationally designed nanoparticles for biomedical applications³ such as highly sensitive assays⁴ and multiplexed imaging.⁵ The stable signals and multiplexing capabilities of these nanoparticles offer an attractive alternative to fluorescence-based techniques.^{6,7} For example, a recent report notes that a SERS-based approach can outperform an enzyme-linked immunosorbent assay (ELISA).⁸ Nanoparticle-based SERS assays could, thus, provide novel sensing capabilities that complement or improve present technologies and lead to next-generation clinical diagnostics. For example, Moskovits *et al.* have extended such studies to quantitatively confirm the ratio of cancerous to noncancerous cells in samples with two different reporter molecule–antibody

* Address correspondence to murphyj@illinois.edu, rxb@illinois.edu.

Received for review September 24, 2012 and accepted February 25, 2013.

Published online February 25, 2013
10.1021/nn305710k

© 2013 American Chemical Society

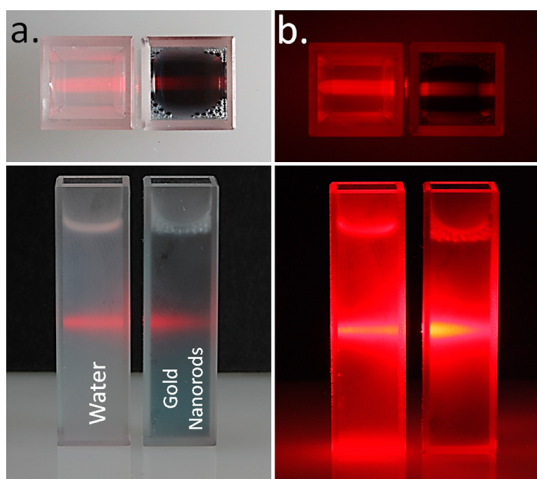


Figure 1. Photographs demonstrating extinction effects in solution. Upon laser illumination, minimal extinction (scattering + absorption) is observed in water (left cuvette). In contrast, suspensions of gold nanorods in water exhibit extinction under illumination (right cuvette). (a) Laser illumination under ambient lighting. (b) Laser illumination without ambient lighting.

combinations.⁹ Using labeled nanoparticles as Raman reporters to achieve contrast in deep-tissue measurements is currently an active area of research.^{10,11}

Light scattering, absorption, and fluorescence arising from the tissue limit the choice of Raman excitation wavelengths to the near-infrared (NIR) spectral region.¹² In this spectral region (700–1100 nm), gold nanorods¹³ and nanoshells¹⁴ can be used as effective SERS-active nanoparticles as they exhibit a tunable plasmon band¹⁵ where tissue has low absorption.¹² Additionally, the presence of the nanoparticles dispersed throughout the tissue adds absorption and scattering effects to the Raman measurement as the light propagates. In this way, nanoparticles that would be injected into tissue behave much like in colloidal suspensions.

For suspensions, as opposed to substrates, accounting for light propagation and attenuation is vital. While the resonant plasmon helps to enhance the Raman signal, attenuation by absorption and scattering complicates experimental design and optimization.¹⁶ Upon plasmonic excitation for anisotropic shapes like rods, the maximum electric field, on average, is at the tips of the rods; therefore, SERS signals will be dominated by events at the tips of the rods. The overall extinction of the nanorods depends not only on their shape but also on their absolute size: larger nanorods, for the same aspect ratio, lead to more extinction, with little relation to the qualities of the rod tips. Therefore, it is not a surprise that, in colloidal solution, SERS and extinction effects need to be unraveled.

This effect is clearly visible in a solution of nanoparticles. For example, Figure 1 shows a photograph of a laser beam traversing two cuvettes, illustrating extinction effects in solution. The cuvette on the left in both

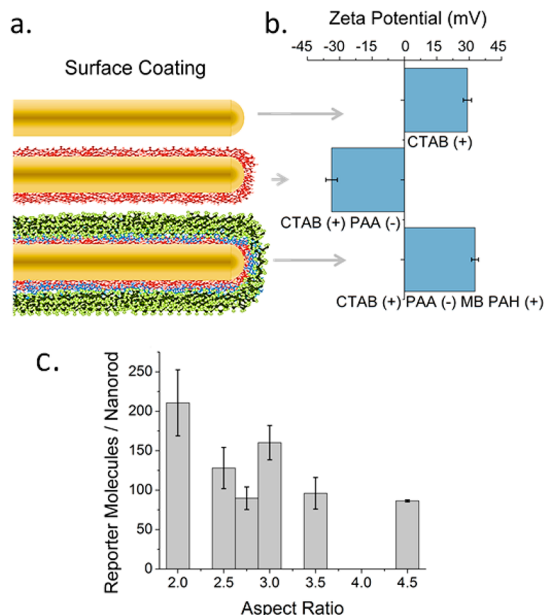


Figure 2. (a) Schematic of a gold nanorod with a (red) poly(acrylic acid) coating, followed by methylene blue reporter molecules (blue) and a polyallylamine hydrochloride (green) trap coat. (b) Corresponding zeta-potential for aspect ratio 3 gold nanorods as a function of layer coating corresponding to the stages in (a). (c) Quantification of the number of methylene blue reporter molecules per gold nanorod as a function of aspect ratio.

panels, containing water, displays minimal scattering and absorption, resulting in minor attenuation of the laser beam. The cuvette on the right, containing gold nanorods in suspension, shows that the laser beam is unable to penetrate effectively through the cuvette, due to a combination of absorption and scattering of light by the nanorods. Therefore, when performing SERS experiments on such nanorods in solution, Raman-scattered light would be similarly extinguished. Therefore, it is important to understand that there is an antagonistic interplay between extinction and SERS enhancement in the observed Raman signal collected from colloidal suspensions and therefore in biological sensing.

Here we explore the competition between SERS enhancement and extinction on propagation through the sample. We investigate the dependence on plasmon resonance frequency by using gold nanorods of six different aspect ratios which provide longitudinal surface plasmon resonances at wavelengths spanning 600–800 nm. The Raman reporter, methylene blue, was trap-coated with a polyelectrolyte layer near the surface of each nanorod. SERS spectra were acquired using a 785 nm excitation wavelength in transmission mode. In order to compare signals across batches of nanorods, the average number of reporter molecules per nanorod was quantified using electrospray ionization liquid chromatography mass spectrometry (ESI-LC-MS). We report the Raman signal per nanorod as a function of aspect ratio, correcting for the attenuation

due to extinction in suspension using methanol as an internal standard.

RESULTS AND DISCUSSION

SERS measurements are typically based on Raman reporter molecules attached directly to the surface of the nanoparticles by either covalent or electrostatic interactions.¹⁷ Other reports have examined the use of SERS using reporter molecules separated at fixed distances from the surface of the nanoparticles by employing a dielectric silica shell.¹⁸ Here, we utilize a polyelectrolyte dielectric layer to wrap gold nanorods of a variety of aspect ratios.¹⁹ A schematic of this technique is illustrated in Figure 2a. First, positively charged CTAB-capped gold nanorods were wrapped with negatively charged poly(acrylic acid) (PAA). We then attached methylene blue reporter molecules by electrostatic interactions. The reporter molecules were then trap-coated by an additional polyallylamine hydrochloride (PAH) polyelectrolyte layer.²⁰ Layer wrapping was confirmed at each step by zeta-potential measurements (Figure 2b) and electronic absorption spectra as previously described.²¹ Shifts in the longitudinal plasmon peak of 5 nm or less are observed as the surface functionalization proceeds (Supporting Information Figure S1). The polyelectrolyte coating also stabilizes the as-synthesized CTAB-capped gold nanorods from aggregating in polar protic solvents.²² As an approximate guide, assuming a 2.5 nm thick CTAB bilayer and 1.5 nm thicknesses for the polyelectrolyte layers,^{19,21} the Raman reporter dyes should be about 4 nm from the metal surface. There is no apparent aggregation in solution, as suggested by the lack of plasmon band broadening. In the case that two nanorods are in contact, the spacer layers guarantee that the reporter molecule is approximately 4 nm away from the proximal metal surface and about 12 nm away from the distal metal surface. Although we cannot rigorously prove that there are zero aggregates in solution, these relative distances suggest that the reporter molecules are not expected to lie in hot spots.

The number of reporter molecules per nanorod was quantified for each aspect ratio by ESI-LC-MS.²¹ We found that the average number of reporters per gold nanorod was 100–300 reporter molecules (Figure 2c). These ESI-LC-MS measurements were carried out in triplicate for three independent batches, for each aspect ratio of nanorods. The means of 9 measurements per aspect ratio, with attendant error bars of one standard deviation from the means, are shown in Figure 2c with further details in Figure S2. The values of 100–300 reporters per nanorod are far fewer than monolayer coverage. For example, methylene blue adsorbs to charged surfaces from water with a footprint of 0.66 nm^{2,23} A full monolayer of methylene blue, hence, would imply approximately 3000 molecules per nanorod. Therefore,

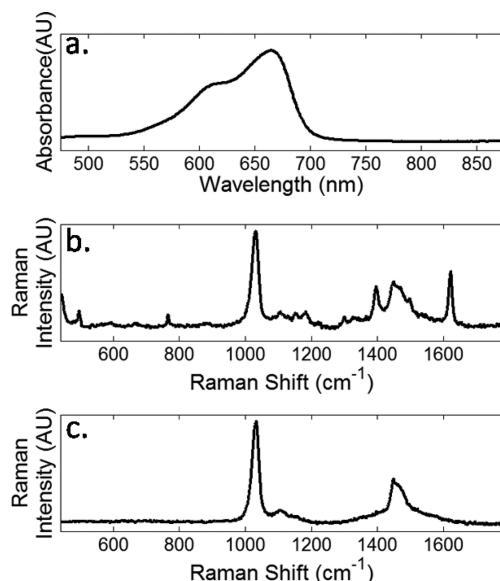


Figure 3. Reference spectra. (a) UV/vis of 15 μM methylene blue in methanol. (b) Raman spectrum of 500 μM methylene blue in methanol. (c) Raman spectrum of neat methanol.

experimental loadings are less than 10% of monolayer coverage. Using these values, we compare the experimentally observed SERS signal intensity from each gold nanorod suspension and relate them to theory.

To characterize the observed spectral signatures, we present three reference spectra in Figure 3. The electronic absorption spectrum of methylene blue in methanol is shown in Figure 3a. An absorption maximum can be seen around 670 nm with a shoulder at 650 nm, both of which are blue-shifted from the Raman laser excitation wavelength of 785 nm. This should minimize any chemical resonance effects such as those observed in surface-enhanced resonance Raman spectroscopy (SERRS).

For Raman measurements, we collected the signal from a sample of methylene blue polyelectrolyte-coated gold nanorods resuspended in methanol. This approach was first introduced by Kneipp and co-workers²⁴ and has the benefit that the methanol Raman band at 1030 cm^{-1} ²⁵ can serve as an internal standard. For reference, the Raman spectra of methylene blue in methanol and of neat methanol are shown in Figure 3b,c.

We synthesized gold nanorods with aspect ratios from 2 to 4.5, resulting in a systematic variation of the longitudinal plasmon resonance band. Figure 4a shows the electronic absorption spectra of each of the gold nanorod suspensions after the final PAH polyelectrolyte trap coating. On the same spectral axes, we also depict the laser excitation wavelength with a red dotted line and the resulting Raman spectrum (black curve) for reference. Traditionally, Raman spectra are reported in terms of Raman shift from an excitation wavelength, as shown in Figure 4b, where the spectra are normalized for concentration and the number of reporter molecules per rod and then offset for clarity. From the shaded region in Figure 4a, it is obvious that

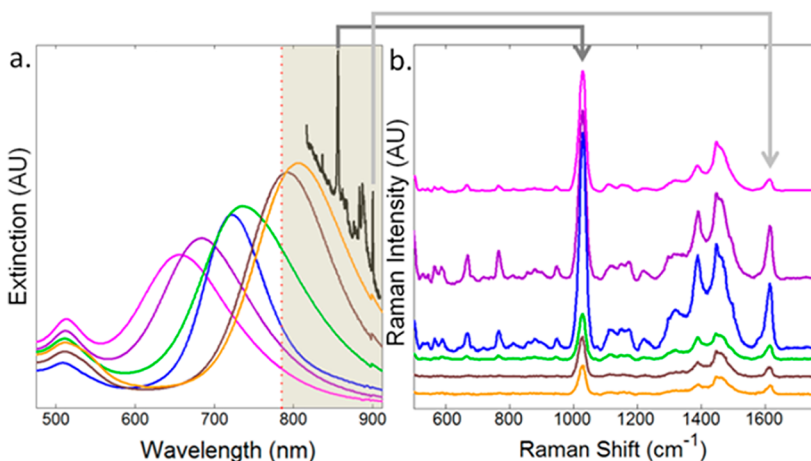


Figure 4. (a) Extinction spectra for gold nanorods (AR 2, pink; AR 2.5, purple; AR 2.75, blue; AR 3, green; AR 3.5, brown; and AR 4.5, orange), normalized to concentration plotted on the same axes as the position of the Raman excitation wavelength (red dots) and the resulting Raman spectrum (black). The spectral region shown in Figure 5b is highlighted by shadow in Figure 5a. (b) Surface-enhanced Raman spectrum of methylene blue attached to six different aspect ratios of gold nanorods bearing PAA polyelectrolyte layer (offset for clarity) normalized for gold nanorods and reporter molecule concentration.

the extinction profile of higher aspect ratio nanorods in suspension overlaps both the spectral profile of the Raman excitation laser and the wavelengths of Raman scattered photons. The largest Raman signal is observed for nanorods that have a plasmon band blue-shifted from the excitation frequency. To quantify the recorded signal, we examined both the reporter Raman signal as well as that of the suspending medium (methanol).

Two spectral features to characterize our suspensions are the Raman band originating from methanol at 1030 cm^{-1} shift and the Raman band originating from methylene blue at 1616 cm^{-1} shift (Figure 5).²⁶ The signal intensity at 1030 cm^{-1} shift should only decrease from extinction of the Raman excitation wavelength since we assume methanol is not enhanced by the gold nanorods.²⁴ However, the Raman signal from the reporter at 1616 cm^{-1} shift will be affected by the location of the longitudinal surface plasmon resonance determined by the aspect ratio of the gold nanorod suspensions. By examining these two bands as a function of aspect ratio, we illustrate the effects of the competing physical processes. In addition, we can select an aspect ratio that would provide the largest Raman signal in suspension.

Extinction measurements (Figure 4a) and Raman measurements of the methanol band (Figure 5) provided two estimates of the extinction due to nanorods. This extinction is quantified in Figure 6a. The competing process of SERS electromagnetic enhancement when extinction effects are considered to be negligible (*i.e.*, substrate measurements) is presented in Figure 6b. A prolate-spheroidal approximation for the rods was used to estimate absorption-free electromagnetic enhancement.²⁷ It is clear from Figure 6 that maximum extinction of the Raman excitation occurs near the

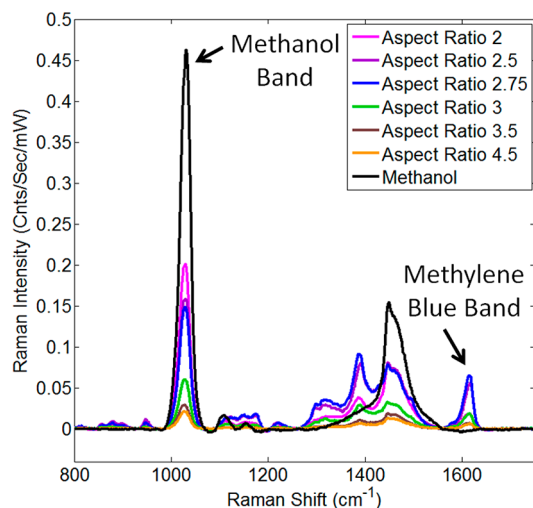


Figure 5. Comparison of Raman spectra acquired from gold nanorod suspensions bearing polyelectrolyte layers plus methylene blue reporter in methanol. The variation in Raman intensity for the methanol bands is illustrated by the peak at 1030 cm^{-1} which varies as a function of aspect ratio. Gold nanorod suspensions are normalized for concentration and the number of reporter molecules per gold nanorod.

maximum of electromagnetic enhancement. The collected signal seen in Figure 5 illustrates this competition.

As the SERS signal will vary as a function of the nanoparticle concentration and the number of reporter molecules per nanoparticle, it is important to account for these variations in order to understand the spectral data. Using theory, we account for these experimental variations between samples. The observed Raman spectra are quantified using the reporter signal at 1616 cm^{-1} shift for each aspect ratio. These results are shown in Figure 7. The normalized Raman signal in transmission mode from a suspension of gold nanorods can be shown to be equal to¹⁶

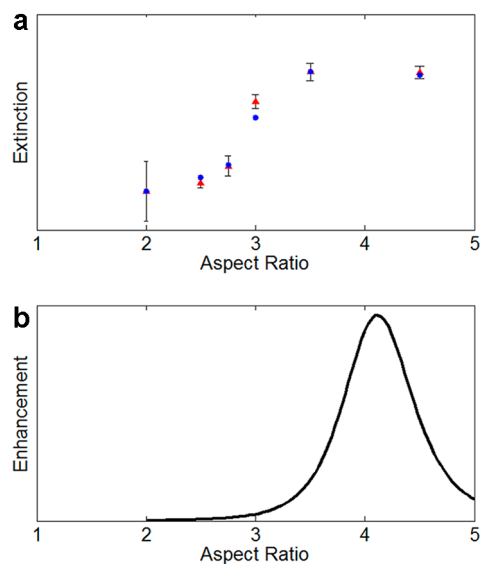


Figure 6. (a) Blue dots: Experimentally observed extinction of Raman excitation at 785 nm. Red triangles: Difference in Raman band at 1030 cm^{-1} shift with neat methanol and each aspect ratio of gold nanorods suspended in methanol. (b) Predicted electromagnetic enhancement from varying aspect ratios of spheroids in the quasi-static limit. Mean-free electron path and depolarization/radiative damping corrections were applied.

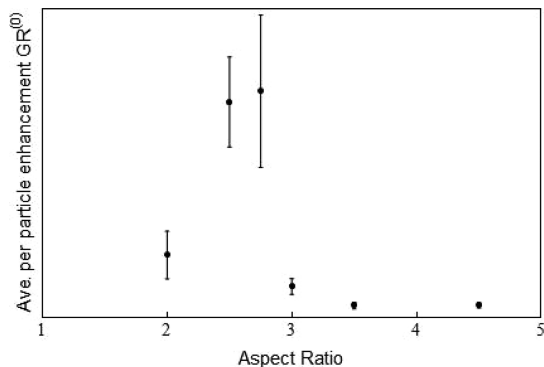


Figure 7. Determined average per particle extinction-modified enhancement factor $GR^{(0)}$ (G as a function of aspect ratio) from eq 2; some error bars are smaller than the data points.

$$R(\omega, \omega_0, \rho, h) = AR^{(0)}\langle G_N(\omega, \omega_0) \rangle \frac{e^{-mC_{ext}(\omega_0)hp} - e^{-mC_{ext}(\omega)hp}}{mC_{ext}(\omega) - mC_{ext}(\omega_0)} \quad (1)$$

where the frequencies ω_0 and ω correspond to the incident light and the Stokes' shifted frequencies, respectively, A is the effective cross-sectional area of the illuminating and collecting beams, $R^{(0)}$ is the Raman signal from a single reporter molecule absent the nanorod, ρ is the concentration of the nanorods in the solution, N indicates the number of bound Raman

reporter molecules, h is the interaction path length, C_{ext} is the extinction cross section of the individual nanorods, m is the refractive index of the solution, and $\langle G_N(\omega, \omega_0) \rangle$ is the ensemble-averaged extinction-modified enhancement factor. The ratio in eq 1 models the propagation of incident light and Raman scattered light through the suspension and is a form of Beer's Law. This expression can be simplified if the number of reporter molecules is small, in which case the ensemble-averaged, extinction-modified enhancement factor $\langle G_N(\omega, \omega_0) \rangle$ can be linearized, that is, $\langle G_N(\omega, \omega_0) \rangle = \langle G(\omega, \omega_0)N \rangle = \langle G(\omega, \omega_0) \rangle N$. This allows us to obtain the averaged per particle extinction-modified enhancement factor.

$$\langle G(\omega, \omega_0) \rangle = \frac{R(\omega, \omega_0, \rho, h)}{R^{(0)}\langle N \rangle} \frac{mC_{ext}(\omega) - mC_{ext}(\omega_0)}{e^{-mC_{ext}(\omega_0)hp} - e^{-mC_{ext}(\omega)hp}} \quad (2)$$

The single-particle, extinction-modified enhancement factor was computed using eq 2 and is shown in Figure 7. A maximum per-particle signal enhancement is found at an aspect ratio of 2.75, with 2.5 also within error bounds. This implies that maximum observed signal occurs with gold nanorods blue-shifted from the laser excitation wavelength. This differs from the field enhancement maximum expected at an aspect ratio of 4.

CONCLUSION

In contrast to SERS experiments of immobilized nanoparticle substrates, where absorption effects are minimal, a significant extinction contribution is realized for SERS particles in suspension. In analyzing the signal generation and recording rigorously, we have demonstrated that Raman-active molecules do not provide monolayer coverage of our polyelectrolyte-bearing nanorods as usually assumed. In our experiments, loadings are less than 10% of the expected maximum for monolayer coverage. The calculated ensemble-average signal intensity based on experimentally determined molecular coverage suggests the maximum Raman scattered signal is obtained from that plasmon resonance that is blue-shifted from excitation. This implies the use of nanorods of lower aspect ratios for optimal sensing. Extinction is an important consideration in combination with maximal SERS enhancement when designing tagged Raman probes for suspension applications such as collecting Raman reporter signal through tissue. Efforts toward refining our model by accurately spatially localizing reporter binding sites on the gold nanorods are currently underway in our laboratories.

MATERIALS AND METHODS

Materials. Hydrogen tetrachloroaurate(III) hydrate ($\text{HAuCl}_4 \cdot 3\text{H}_2\text{O}$, >99.99%), sodium borohydride (NaBH_4 , 99.99%), and silver

nitrate (AgNO_3 , >99.0%) were obtained from Aldrich and used as received. Methylene blue (>82%) with the remainder in organic salts, cetyltrimethylammonium bromide (CTAB, >99%), and ascorbic acid ($\text{C}_6\text{H}_8\text{O}_6$, >99.0%) were obtained from Sigma

Chemical and used as received. The polyelectrolytes poly(acrylic acid), sodium salt, $M_w \sim 15\,000$ g/mol (35 wt % solution in H₂O) (PAA), and polyallylamine hydrochloride, $M_w \sim 15\,000$ g/mol (PAH), were obtained from Aldrich and used without further purification. Sodium chloride (NaCl, >99.0%) was obtained and used as received from Fischer Chemicals. All solutions were prepared using Barnstead E-Pure 18 MΩ·cm water. All glassware used was cleaned with aqua regia and finally rinsed with 18 MΩ·cm water.

Gold Nanorod Synthesis. CTAB-coated gold nanorods of aspect ratio (AR) 2, 2.5, 2.75, 3, 3.5, and 4.5 corresponding to dimensions 35 ± 2 nm × 17 ± 1 nm, 39 ± 6 nm × 16 ± 4 nm, 40 ± 5 nm × 14 ± 2 nm, 43 ± 4 nm × 15 ± 1 nm, 45 ± 3 nm × 12 ± 1 nm, and $48 \pm 3 \times 11 \pm 1$ nm were synthesized as previously described.²⁸ The gold nanorods were purified twice by centrifugation (8000 rpm, 2 h).

Polyelectrolyte Layer-by-Layer (LBL) Coating. We coated the gold nanorods with PAA and PAH using an adapted procedure¹⁹ to maintain the nanoparticle concentration throughout each step. For each polyelectrolyte layer, we prepared stock aqueous solutions of PAA (–) or PAH (+) at concentrations of 10 mg/mL prepared in 1 mM NaCl and a separate aqueous solution of 10 mM NaCl. To 30 mL aliquots of twice centrifuged CTAB gold nanorods (0.15 nM in particles) we added 6 mL of PAA or PAH (+) solution followed by 3 mL of 10 mM NaCl. The solutions were left to complex overnight (12–16 h) before purification using centrifugation (5000 rpm, 2 h). We then centrifuged the supernatant and concentrated the two pellets to minimize losses in gold nanorod concentration. Zeta-potential measurements and UV–vis absorption measurements were made between each layering step to confirm successful coating without aggregation of the gold nanorods.

Zeta potentials were measured on a Brookhaven ZetaPALS instrument. Absorption spectra were recorded on a Cary 500 UV–vis–NIR spectrometer, and transmission electron microscope images were taken on a JEOL 2100 cryo-TEM microscope at a 200 kV accelerating voltage. All TEM grids were prepared by drop-casting 10 μL of purified gold nanorods on a holey carbon TEM grid (Pacific Grid-Tech). A ThermoScientific Sorvall Legend X1 centrifuge in a “swinging bucket” orientation was used for purification as detailed below.

Methylene Blue Gold Nanorod Complexation. We used the same initial concentration of gold nanorods (0.15 nM) prior to addition of 10 μL of a stock 1 mM methylene blue solution to 0.99 mL of gold nanorods, to give a final methylene blue concentration of 1 μM during complexation. The mixture was left for an hour before removing excess reporter molecules using centrifugation (2350 rcf, 15 min). The supernatant was also centrifuged, and both pellets were concentrated to maintain gold nanorod concentration. The concentrated pellet was then resuspended to 1 mL with DI water before adding 0.2 mL of PAH (10 mg/mL) in 1 mM NaCl and 0.1 mL of 10 mM aqueous NaCl solutions. This mixture was left overnight before purification by centrifugation (2350 rcf, 15 min); again, the supernatant was also centrifuged (2350 rcf, 15 min), and the pellets were concentrated. For final purification, we dialyzed the aqueous solutions in Spectrum Laboratories 100k MWCO G2 membranes against 4 L of Barnstead E-Pure (18 MΩ·cm) water for 48 h. Any remaining unbound methylene blue molecules and excess polyelectrolyte were removed via centrifugation followed by dialysis in a 100 kDa cutoff membrane. By using a membrane pore size 5 times larger than the molecular weight of the polyelectrolyte used, any multilayer polyelectrolyte bundles that may have formed during synthesis should be removed.

ESI-LC-MS Quantification of Methylene Blue. For electrospray ionization liquid chromatography mass spectrometry (ESI-LC-MS) quantification of the number of methylene blue molecules, we centrifuged the methylene blue complexed polyelectrolyte gold nanorods (2350 rcf, 15 min) and the supernatant again (2350 rcf, 15 min) before concentrating the pellets. We resuspended the pellet in 50 μL of methanol, and the gold nanorod cores were then etched by adding 0.010 mL of 1 M KCN and waiting 1–2 h. It was observed that etching had completed once the solution turned colorless. KCN itself does not disturb the mass spectral analysis of methylene blue (see Supporting Information).

All data in Figure 2c are the results of triplicate measurements for each of three independent batches of nanorods for each aspect ratio.

The ESI-LC-MS analysis was performed in Metabolomics Center at UIUC with a 5500 QTRAP mass spectrometer (AB Sciex, Foster City, CA) which is equipped with a 1200 Agilent LC Analyst (version 1.5.1, Applied Biosystems) was used for data acquisition and processing. An Agilent Zorbax SB-Aq column (5 μ, 50 × 4.6 mm) was used for the separation. The HPLC flow rate was set at 0.3 mL/min. HPLC mobile phases consisted of A (0.1% formic acid in H₂O) and B (0.1% formic acid in acetonitrile). The gradient was as follows: 0–1 min, 98% A; 6–10 min, 2% A; 10.5–17 min, 98% A. The autosampler was kept at 5 °C. The injection volume was 1 μL. The mass spectrometer was operated with positive electrospray ionization. The electrospray voltage was set to 2500 V; the heater was set at 400 °C; the curtain gas was 35, and GS1 and GS2 were 50 and 55, respectively. Quantitative analysis was performed via multiple reaction monitoring (MRM) where *m/z* 284.2 to 240.1 for methylene blue was monitored. Calibration curves were run on methylene blue standards in the presence of cyanide, from 0.01 to 0.1 μM concentrations; our data found 0.029–0.108 μM concentrations (Figure S2).

Raman Spectroscopy. For Raman acquisition, the dialyzed gold nanorod samples were centrifuged to concentrate the pellets (2350 rcf, 15 min) and the supernatant poured off. The samples were then resuspended in 2 mL of methanol (HPLC Fischer Scientific, >99.9% purity) and placed in a quartz cuvette. Triplicate samples were synthesized, with seven spectral acquisitions of each sample collected to minimize the signal-to-noise ratio.

Raman spectra were acquired on liquid samples in transmission mode (LabRAM, Horiba). The excitation wavelength for all measurements was 785 nm with a 30 s acquisition time. The Raman shift from 400 to 1800 cm⁻¹ was collected at ~9 cm⁻¹ spectral resolution. Laser light was focused through a 1 cm path length cuvette with a 40 mm focal length lens and collected with a 125 mm focal length lens to collimate the transmitted light and direct it to the spectrograph. Laser power at the sample was 25 mW. Between measurements, the cuvette was rinsed with aqua regia (3:1 HCl/HNO₃) followed by multiple rinses with Barnstead E-Pure (18 MΩ·cm) water and methanol. For Raman measurements, the gold nanorod concentrations were 0.36, 0.36, 0.31, 0.33, 0.33, and 0.29 nM for aspect ratios 2, 2.5, 2.75, 3, 3.5, and 4.5, respectively, necessitating a small correction to the recorded data which did not change the relative trend observed in the Raman spectra between aspect ratios. Electronic absorption spectra were confirmed before and after Raman measurements.

Conflict of Interest: The authors declare no competing financial interest.

Acknowledgment. S.T.S. and B.M.D. acknowledge support from the University of Illinois at Urbana—Champaign from NIH National Cancer Institute Alliance for Nanotechnology in Cancer “Midwest Cancer Nanotechnology Training Center” Grant R25 CA154015A. M.V.S. acknowledges support through the Congressionally Directed Medical Research Program Postdoctoral Fellowship BC101112. We also acknowledge support from a Beckman Institute seed grant, AFOSR Grant No. FA 9550-09-1-0246 and NSF Grant Nos. CHE-1011980 and CHE 0957849. The authors thank the Roy J. Carver Biotechnology Metabolomics Center at the University of Illinois at Urbana—Champaign for mass spectrometry analysis.

Supporting Information Available: Additional characterization details of mass spectrometry and electronic absorption between synthetic steps. This material is available free of charge via the Internet at <http://pubs.acs.org>.

REFERENCES AND NOTES

- Haynes, C. L.; McFarland, A. D.; Van Duyne, R. P. Surface-Enhanced Raman Spectroscopy. *Anal. Chem.* **2005**, *77*, 338A–346A.
- McFarland, A. D.; Young, M. A.; Dieringer, J. A.; Van Duyne, R. P. Wavelength-Scanned Surface-Enhanced Raman Excitation Spectroscopy. *J. Phys. Chem. B* **2005**, *109*, 11279–11285.

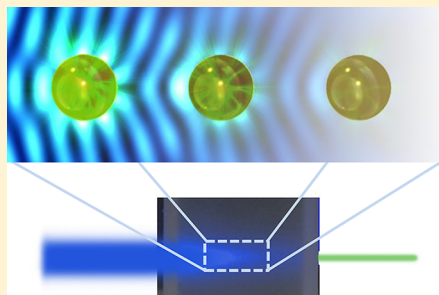
3. Banholzer, M. J.; Millstone, J. E.; Qin, L.; Mirkin, C. A. Rationally Designed Nanostructures for Surface-Enhanced Raman Spectroscopy. *Chem. Soc. Rev.* **2008**, *37*, 885–897.
4. Porter, M. D.; Lipert, R. J.; Siperko, L. M.; Wang, G.; Narayananan, R. SERS as a Bioassay Platform: Fundamentals, Design, and Applications. *Chem. Soc. Rev.* **2008**, *37*, 1001–1011.
5. Kodali, A. K.; Llora, X.; Bhargava, R. Optimally Designed Nanolayered Metal-Dielectric Particles as Probes for Massively Multiplexed and Ultrasensitive Molecular Assays. *Proc. Natl. Acad. Sci. U.S.A.* **2010**, *107*, 13620–13625.
6. Zavaleta, C. L.; Smith, B. R.; Walton, I.; Doering, W.; Davis, G.; Shojaei, B.; Natan, M. J.; Gambhir, S. S. Multiplexed Imaging of Surface Enhanced Raman Scattering Nanotags in Living Mice Using Noninvasive Raman Spectroscopy. *Proc. Natl. Acad. Sci. U.S.A.* **2009**, *106*, 13511–13516.
7. Xing, Y.; Chaudry, Q.; Shen, C.; Kong, K. Y.; Zhai, H. E.; Wchung, L.; Petros, J. A.; O'Regan, R. M.; Yezhelyev, M. V.; Simons, J. W.; et al. Biocomjugated Quantum Dots for Multiplexed and Quantitative Immunohistochemistry. *Nat. Protoc.* **2007**, *2*, 1152–1165.
8. Wang, G.; Lipert, R. J.; Jain, M.; Kaur, S.; Chakraboty, S.; Torres, M. P.; Batra, S. K.; Brand, R. E.; Porter, M. D. Detection of the Potential Pancreatic Cancer Marker MUC4 in Serum Using Surface-Enhanced Raman Scattering. *Anal. Chem.* **2011**, *83*, 2554–2561.
9. Pallaoro, A.; Braun, G. B.; Moskovits, M. Quantitative Ratio-metric Discrimination between Noncancerous and Cancerous Prostate Cells Based on Neuropilin-1 Overexpression. *Proc. Natl. Acad. Sci. U.S.A.* **2011**, *108*, 16559–16564.
10. Stone, N.; Faulds, K.; Graham, D.; Matousek, P. Prospects of Deep Raman Spectroscopy for Noninvasive Detection of Conjugated Surface Enhanced Resonance Raman Scattering Nanoparticles Buried within 25 mm of Mammalian Tissue. *Anal. Chem.* **2010**, *82*, 3969–3973.
11. Stone, N.; Kerssens, M.; Lloyd, G. R.; Faulds, K.; Graham, D.; Matousek, P. Surface Enhanced Spatially Offset Raman Spectroscopic (SEORS) Imaging—The Next Dimension. *Chem. Sci.* **2011**, *2*, 776–780.
12. Richards-Kortum, R.; Sevick-Muraca, E. Quantitative Optical Spectroscopy for Tissue Diagnosis. *Annu. Rev. Phys. Chem.* **1996**, *47*, 555–606.
13. Huang, X.; El-Sayed, I. H.; Qian, W.; El-Sayed, M. A. Cancer Cells Assemble and Align Gold Nanorods Conjugated to Antibodies To Produce Highly Enhanced, Sharp, and Polarized Surface Raman Spectra: A Potential Cancer Diagnostic Marker. *Nano Lett.* **2007**, *7*, 1591–1597.
14. Lal, S.; Grady, N. K.; Kundu, J.; Levin, C. S.; Lassiter, J. B.; Halas, N. J. Tailoring Plasmonic Substrates for Surface Enhanced Spectroscopies. *Chem. Soc. Rev.* **2008**, *37*, 898–911.
15. Jain, P. K.; Huang, X.; El-Sayed, I. H.; El-Sayed, M. A. Noble Metals on the Nanoscale: Optical and Photothermal Properties and Some Applications in Imaging, Sensing, Biology, and Medicine. *Acc. Chem. Res.* **2008**, *41*, 1578–1586.
16. van Dijk, T.; Sivapalan, S. T.; DeVetter, B. M.; Yang, T. K.; Schulmerich, M. V.; Murphy, C. J.; Bhargava, R.; Carney, P. S. Competition between extinction and enhancement in surface enhanced Raman spectroscopy. **2013**, arXiv:1303.0277.
17. Guerrini, L.; Jurasekova, Z.; Domingo, C.; Perez-Mendez, M.; Leyton, P.; Campos-Vallette, M.; Garcia-Ramos, J. V.; Sanchez-Cortes, S. Importance of Metal-Adsorbate Interactions for the Surface-Enhanced Raman Scattering of Molecules Adsorbed on Plasmonic Nanoparticles. *Plasmonics* **2007**, *2*, 147–156.
18. Li, J. F.; Huang, Y. F.; Ding, Y.; Yang, Z. L.; Li, S. B.; Zhou, X. S.; Fan, F. R.; Zhang, W.; Zhou, Z. Y.; Wu, D. Y.; et al. Shell-Isolated Nanoparticle-Enhanced Raman Spectroscopy. *Nature* **2010**, *464*, 392–395.
19. Gole, A.; Murphy, C. J. Polyelectrolyte-Coated Gold Nanorods: Synthesis, Characterization and Immobilization. *Chem. Mater.* **2005**, *17*, 1325–1330.
20. Huang, J. Y.; Jackson, K. S.; Murphy, C. J. Polyelectrolyte Wrapping Layers Control Rates of Photothermal Molecular Release from Gold Nanorods. *Nano Lett.* **2012**, *12*, 2982–2987.
21. Sivapalan, S. T.; Vella, J. H.; Yang, T. K.; Dalton, M. J.; Swiger, R. N.; Haley, J. E.; Cooper, T. M.; Urbas, A. M.; Tan, L. S.; Murphy, C. J. Plasmonic Enhancement of the Two Photon Absorption Cross Section of an Organic Chromophore Using Polyelectrolyte-Coated Gold Nanorods. *Langmuir* **2012**, *28*, 9147–9154.
22. Alkilany, A. M.; Thompson, L. B.; Murphy, C. J. Polyelectrolyte Coating Provides a Facile Route To Suspend Gold Nanorods in Polar Organic Solvents and Hydrophobic Polymers. *ACS Appl. Mater. Interfaces* **2010**, *2*, 3417–3421.
23. Hahner, G.; Marti, A.; Spencer, N. D.; Caseri, W. R. Orientation and Electronic Structure of Methylene Blue on Mica: A Near Edge X-ray Absorption Fine Structure Spectroscopy Study. *J. Chem. Phys.* **1996**, *104*, 7749–7757.
24. Kneipp, K.; Dasari, R. R.; Wang, Y. Near-Infrared Surface-Enhanced Raman Scattering (NIR SERS) on Colloidal Silver and Gold. *Appl. Spectrosc.* **1994**, *48*, 951–957.
25. Dixit, S.; Poon, W. C. K.; Crain, J. Hydration of Methanol in Aqueous Solutions: A Raman Spectroscopic Study. *J. Phys.: Condens. Matter* **2000**, *12*, L323–L328.
26. Naujok, R. R.; Duevel, R. V.; Corn, R. M. Fluorescence and Fourier-Transform Surface-Enhanced Raman-Scattering Measurements of Methylene-Blue Adsorbed onto a Sulfur-Modified Gold Electrode. *Langmuir* **1993**, *9*, 1771–1774.
27. Schatz, G. C.; Van Duyne, R. P. Electromagnetic Mechanism of Surface-Enhanced Spectroscopy. In *Handbook of Vibrational Spectroscopy*; John Wiley & Sons, Ltd.: Chichester, UK, 2002; Vol. 1; pp 759–774.
28. Sau, T. K.; Murphy, C. J. Seeded High Yield Synthesis of Short Au Nanorods in Aqueous Solution. *Langmuir* **2004**, *20*, 6414–6420.

Competition Between Extinction and Enhancement in Surface-Enhanced Raman Spectroscopy

Thomas van Dijk,[†] Sean T. Sivapalan,[‡] Brent M. DeVetter,[¶] Timothy K. Yang,[§]
Matthew V. Schulmerich,^{†,||} Catherine J. Murphy,^{‡,§} Rohit Bhargava,^{†,||,⊥} and P. Scott Carney*,^{†,¶}

[†]Beckman Institute for Advanced Science and Technology, [‡]Department of Materials Science and Engineering, [¶]Department of Electrical and Computer Engineering, [§]Department of Chemistry, ^{||}Department of Bioengineering, and [⊥]Department of Mechanical Science and Engineering, Chemical and Biomolecular Engineering and University of Illinois Cancer Center, University of Illinois at Urbana-Champaign, Urbana, Illinois 61801, United States

ABSTRACT: Conjugated metallic nanoparticles are a promising means to achieve ultrasensitive and multiplexed sensing in intact three-dimensional samples, especially for biological applications, via surface-enhanced Raman scattering (SERS). We show that enhancement and extinction are linked and compete in a collection of metallic nanoparticles. Counterintuitively, the Raman signal vanishes when nanoparticles are excited at their plasmon resonance, while increasing nanoparticle concentrations at off-resonance excitation sometimes leads to decreased signal. We develop an effective medium theory that explains both phenomena. Optimal choices of excitation wavelength, individual particle enhancement factor, and concentrations are indicated. The same processes that give rise to enhancement also lead to increased extinction of both the illumination and the Raman-scattered light. Nanoparticles attenuate the incident field (blue) and at the same time provide local enhancement for SERS. Likewise, the radiation of the Raman-scattered field (green) is enhanced by the nearby sphere but extinguished by the rest of the spheres in the suspension upon propagation.



SECTION: Physical Processes in Nanomaterials and Nanostructures

Several methods for using surface-enhanced Raman scattering (SERS)¹ have emerged for biomedical applications, ultrasensitive sensing, and multiplexed analyses. In particular, nanoparticles have been the focus of recent efforts toward *in vitro* and *in vivo* molecular sensing.^{2–5} Nanoparticles can dramatically increase the electric field intensity near and at their surface, providing useful SERS-based probes,⁶ especially for deep tissue imaging at varying concentrations.⁷ Typically, a nanostructured particle is bioconjugated and employed in the same manner as conventional fluorescent probes are used for molecular imaging. SERS probes are postulated to offer bright and stable signals and extensive multiplexing,⁸ while it has been assumed that experimental best practice parallels that of fluorescent probes, that is, that one should excite at the strongest resonance and use a high concentration. In fact, it has recently been recognized even in single-particle enhancement of fluorescence that peak signals are observed to be red-shifted from the plasmon reference.⁹ Thus far, the design of nanoparticle-based SERS experiments has focused on maximizing the local electromagnetic field enhancement in or around an individual particle.^{10,11} This strategy fails to take into account the physics of propagation in the bulk medium where the same processes that give rise to enhancement also lead to increased extinction of both the illumination and the Raman-scattered light. Particles provide enhanced fields for Raman scattering, and the same particles form an effective medium with corresponding absorption. The importance of absorption of

the Raman-scattered light is recognized in ref 12. However, they do not describe the necessary link and competition between the enhancement and the extinction. For example, it is commonly known to experimentalists that gold nanospheres exhibit a plasmon resonance at 520 nm and should produce a large local field enhancement when illuminated at 532 nm; yet, no appreciable Raman signal is observed upon 532 nm excitation commonly ascribed to interband transitions in gold.¹³ Away from the plasmon resonance frequency maximum, the Raman signal is again observed and actually increases as the excitation wavelength becomes longer.

In this Letter, we address the issue of extinction by a suspension of nanoparticles in SERS experiments through an effective medium approach. It is shown that extinction and enhancement are tied to each other and compete in such a way that peak signals are acquired off-resonance and that, at any wavelength, an optimal particle concentration exists to maximize the Raman signal. We provide verification of the model with experiments in which the particle concentration is varied.

Propagation of light in a dilute suspension of identical particles is well-approximated by propagation through a

Received: March 6, 2013

Accepted: March 22, 2013

Published: March 22, 2013

homogeneous medium with an effective refractive index \tilde{m} , given by¹⁴

$$\tilde{m} = m \left[1 + i \frac{2\pi\rho}{k^3} S(0) \right] \quad (1)$$

where m is the refractive index of the medium in which the particles are embedded, $k = \omega/c$ is the wavenumber in the medium, ρ is the number of particles per unit volume, and $S(0)$ is the scattering amplitude in the forward direction.¹⁴ The absorption coefficient in a medium with a complex refractive index is $\alpha = 2k \operatorname{Im} \tilde{m}$. For a suspension with small identical particles, the absorption coefficient is given by $\alpha = m4\pi\rho k^{-2} \operatorname{Re}[S(0)] = \rho m C_{\text{ext}}$, where C_{ext} is the extinction cross section of a single particle in the suspension, proportional to the real part of the forward-scattering amplitude. The attenuation of a well-collimated beam propagating through the effective medium is described by Beer's law,¹⁵ $I(h) = I(0)e^{-h\rho C_{\text{ext}}}$, where I is the intensity and h is the propagation distance. The extinction cross section, rather than the absorption cross section, is used to account also for scattering out of the collection and detection optical train or subsequent absorption. Hence, for systems of large particles, where the scattering is mostly in the forward direction, or for high-NA systems, this model may fail or require correction for contribution to the detection by the scattered field. In the system considered here, the particles are small compared to the wavelength, and the optical system is low-NA.¹⁶

The extinction cross section, C_{ext} , for a small metallic sphere with radius a , to terms of order $(ka)^4$, is given by¹⁴

$$C_{\text{ext}} = 4k\pi a^3 \operatorname{Im} \left\{ \frac{p^2 - 1}{p^2 + 2} \left[1 + \frac{(ka)^2}{15} \left(\frac{p^2 - 1}{p^2 + 2} \right) \times \frac{p^2 + 27p^2 + 38}{2p^2 + 3} \right] \right\} + \frac{8}{3} (ka)^4 \times \pi a^2 \operatorname{Re} \left[\left(\frac{p^2 - 1}{p^2 + 2} \right)^2 \right] \quad (2)$$

where $p = m_s/m$ is the ratio of the refractive index of the material of the spheres, m_s , to that of the refractive index of the medium, m , which both depend on the wavenumber. For dilute suspensions, the change in the real part of the refractive index of the effective medium from the background is negligible. The extinction from gold spheres in a suspension is shown in Figure 1, where the extinction peaks near the Fröhlich frequency ($\lambda_f \approx 520$ nm); for this calculation the optical constants obtained by Johnson and Christy for gold have been used.¹⁷

The Raman signal, which we denote as R , from a single, isolated nanoparticle depends on the incident field amplitude, E_0 , the number of Raman-active molecules, N , the local field enhancement, $f(\mathbf{r}, \omega)$, and the spatial distribution of those molecules. This last point we address through a probability density, which in general will also depend on the number of molecules present, $p(\mathbf{r}, N)$. Though not explicitly noted, the local enhancement factor is also dependent on the orientation of the incident electric field vector. The number of molecules attached to the nanoparticle may itself be random and given by the probability of finding N molecules attached to the particle P_N . A single molecule at \mathbf{r} is excited by a field with amplitude $E_0 f(\mathbf{r}, \omega_0)$, producing a secondary source proportional to the

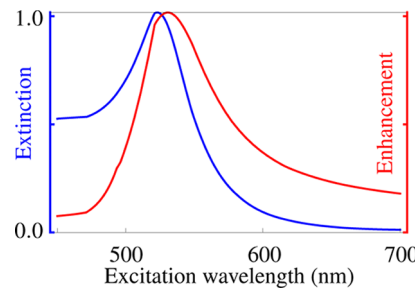


Figure 1. (blue) The normalized extinction cross section C_{ext} from eq 2. Extinction by gold spheres of 5 nm radius in aqueous suspension as a function of the wavelength of the incident light. (red) The normalized Raman enhancement, $G(\lambda)$ from eq 4, versus the excitation wavelength for gold spheres of radius much smaller than the wavelength evaluated for a Raman shift of 0 nm.

Raman susceptibility χ , which implicitly depends on ω_0 and ω . The field reradiated at the Raman-shifted frequency ω is enhanced by the particle as well, so that, by reciprocity, the reradiated field is proportional to $\chi E_0 f(\mathbf{r}, \omega_0) f(\mathbf{r}, \omega)$. We assume that the Raman signal from each reporter molecule is statistically independent; therefore, the intensities add. The ensemble-averaged Raman signal for a single nanoparticle is thus given by

$$R = |\chi|^2 \sum_{N=1}^{\infty} N P_N \int d^3r |E_0 f(\mathbf{r}, \omega_0) f(\mathbf{r}, \omega)|^2 p(\mathbf{r}, N) = \langle N \rangle G^{(0)} \quad (3)$$

where $R^{(0)}$ is the Raman signal from one molecule absent the particle and G is the Raman enhancement factor and generally depends on $p(\mathbf{r}, N)$ and P_N . For systems in which the particle placement is independent of the number of particles, the sum and the integral may be carried out independently, the sum yielding the average number of molecules $\langle N \rangle$, and the integral resulting in a G independent of the number of molecules.

The enhancement factor for a small sphere of radius a ($a \ll \lambda$) with a uniform probability of molecule placement over the surface of the sphere can be calculated in closed form¹⁸

$$G(\omega, \omega_0) = |[1 + 2g(\omega_0)][1 + 2g(\omega)]|^2 \quad (4)$$

where $g = (p^2 - 1)/(p^2 + 2)$, ω_0 is the frequency of the incident field, and ω is the frequency of the Raman-scattered field.

The enhancement calculated by eq 4 is shown in Figure 1 alongside the extinction using the optical constants obtained by Johnson and Christy.¹⁷ It is clear that enhancement and extinction are closely linked and that when the enhancement is strong, the correspondingly strong extinction must be taken into account. The light falling on a single particle is attenuated by propagation through the suspension and arrives with amplitude attenuated by the factor $\exp[-\int_0^z dz' \rho(z') m C_{\text{ext}}(\omega_0)/2]$. The local Raman signal is then $\langle N \rangle R^{(0)} G p(z) \exp[-\int_0^z dz' \rho(z') m C_{\text{ext}}(\omega_0)]$. In transmission mode, this signal must then propagate out through the medium to $z = h$, and the intensity is attenuated by a factor of $\exp[-\int_z^h dz' \rho(z') m C_{\text{ext}}(\omega)]$. The total signal is a sum over the signal from all particles, so that

$$R = \langle N \rangle AR^{(0)} G \int_0^h dz \rho(z) \exp\left[-\int_0^z dz' \rho(z')\right] \\ \times mC_{\text{ext}}(\omega_0)] \exp\left[-\int_z^h dz' \rho(z') mC_{\text{ext}}(\omega)\right] \quad (5)$$

where A is the integral over the transverse beam profile normalized to the peak value, the effective transverse area of the beam. When the concentration $\rho(z)$ does not depend on z , the integrals can be computed in closed form with the result

$$R = \langle N \rangle AR^{(0)} G \frac{e^{-mC_{\text{ext}}(\omega_0)h\rho} - e^{-mC_{\text{ext}}(\omega)h\rho}}{mC_{\text{ext}}(\omega) - mC_{\text{ext}}(\omega_0)} \quad (6)$$

From this expression, it is seen that there are two competing processes that determine the size of the Raman signal, the enhancement, G , and the extinction that results in an exponential decay of the signal. The same processes that increase the enhancement also increase the extinction. The attenuation due to extinction depends not only on the frequency but also on the concentration of the nanospheres. This is illustrated in Figure 2a, where it is shown that for increasing concentration, the peak

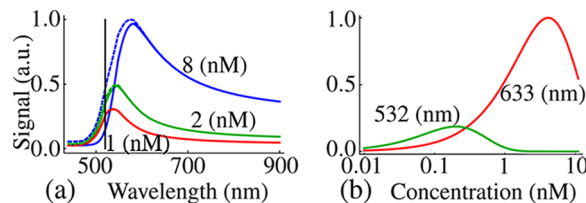


Figure 2. (a) Solid lines: Predicted signal in transmission mode versus the wavelength of the incident light. Dashed lines: Predicted signal in reflection mode versus the wavelength of the incident light. Both transmission and reflection signals are with three different concentrations of the nanospheres that have a radius 6 nm; the sample thickness h is 2 cm. The vertical black line indicates the location of the surface plasmon resonance. (b) Predicted signal in transmission mode versus the concentration for two different incident wavelengths; the radius of the spheres is 15 nm.

of the signal is shifted farther away from the resonant wavelength. This result explains the absence of Raman signal at the plasmon resonance where extinction is so strong that no signal is observed.

In reflection mode, there is always a contribution from the front layer of the sample that is not attenuated, and therefore, the expression for the Raman signal is slightly altered

$$R = \langle N \rangle AR^{(0)} G \frac{1 - e^{-hmp[C_{\text{ext}}(\omega) + C_{\text{ext}}(\omega_0)]}}{mC_{\text{ext}}(\omega) + mC_{\text{ext}}(\omega_0)} \quad (7)$$

The Raman signal in reflection mode for three different concentrations of the nanospheres is shown in Figure 2a as the dashed lines. In the reflection mode, there is a slightly higher signal to the blue side of the resonance compared to the signal in transmission mode.

The Raman signal in transmission mode is depicted in Figure 2b for two commonly used wavelengths evaluated for a Raman band at 1076 cm^{-1} . For $\lambda = 532 \text{ nm}$, the excitation wavelength closest to the plasmon resonance, the signal is very small. A higher signal is found farther away from resonance with the peak shifted to the red. For relatively low concentrations, the biggest signal is obtained with a wavelength of 632 nm . Only for concentrations smaller than 0.1 nM is the signal bigger for the excitation wavelength closest to resonance, as shown in

Figure 2b. It is seen that there is a concentration that maximizes the signal. This optimal concentration, ρ_{opt} , can be found by differentiating eq 6 and equating it to zero, giving the following expression

$$\rho_{\text{opt}} = \frac{\ln[C_{\text{ext}}(\omega)/C_{\text{ext}}(\omega_0)]}{hm[C_{\text{ext}}(\omega) - C_{\text{ext}}(\omega_0)]} \quad (8)$$

When the extinction cross section, $C_{\text{ext}}(\omega)$, equals, or is very close to, $C_{\text{ext}}(\omega_0)$, the optimal concentration becomes $\rho_{\text{opt}} = 1/[hmC_{\text{ext}}(\omega_0)]$. The strong nonlinearity with concentration that these competing phenomena impose on the recorded signal is also a caution in the development of practical assays and must be taken into account to correctly quantify results across samples. Hence, this physics-based analysis enables quantitative molecular imaging for SERS-based microscopy.

The model presented in this paper is validated by measuring the SERS signal of 4,4'-dipyridyl Raman reporter molecules attached to gold nanospheres. Spectra were acquired from the nanoparticles in suspension using a high-resolution Raman spectrometer (LabRAM, Horiba) with a 90 s acquisition time. The Raman shift from 200 to 1800 cm^{-1} was collected at 10 cm^{-1} resolution with 10 mW laser power at the sample. Transmission Raman measurements were collected by focusing laser light through a 1 cm cuvette with a 50 mm focal length lens and collected with a 100 mm focal length lens to collimate the transmitted light and direct it to the spectrograph.

The integrated SERS signal under three different bands (476 , 1076 , and 1600 cm^{-1}) is compared for different concentrations of the gold spheres when excited at 632 nm . The SERS spectra from 4,4'-dipyridyl for increasing concentrations is illustrated in Figure 3a. The three boxes indicate the Raman bands for which

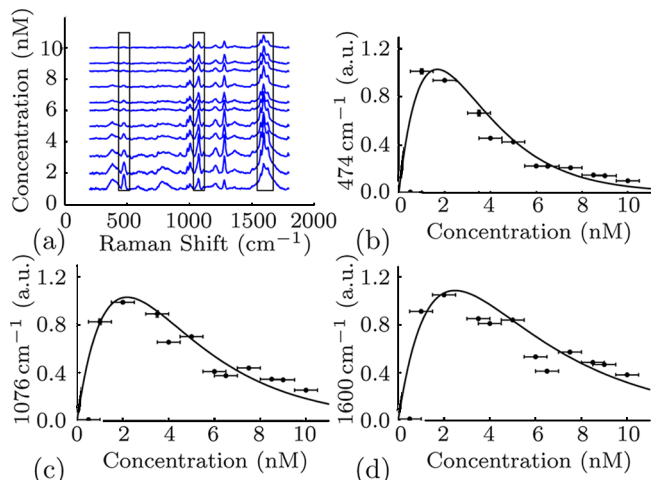


Figure 3. (a) SERS spectra of 4,4'-dipyridyl attached to gold nanospheres with a radius of 15 nm at an excitation wavelength of 633 nm at different nanoparticle concentrations. Measured Raman signals (points) agree with the theoretical prediction (solid line) for a Raman shift of (b) 474 , (c) 1076 , and (d) 1600 cm^{-1} .

the signal is investigated as a function of concentration. The signal is obtained by integrating the Raman band of interest over the width of the box, as shown in Figure 3.

As predicted, increasing the concentration of nanoparticles in an attempt to increase the signal leads to signal attenuation beyond an optimal concentration. The measurements are in good agreement with the model. Our results suggest that strategies to increase Raman signals using nanoparticles should

not focus on achieving greater local enhancement but instead might strive for designs that maximize total signal by separating the single-particle enhancement and absorption peaks or otherwise tailoring the shape of the enhancement and absorption curves to maximize the gap between absorption and enhancement at frequencies away from resonance. A move toward using thin samples with large areas of collection is also suggested. We see that the signal is increased by moving away from resonance and, in some cases, by lowering the concentration of particles. While we focused on nanospheres, our results apply broadly to particle-based Raman enhancement with nonspherical particles as well.

■ EXPERIMENTAL METHODS

Gold nanospheres of 15 nm radius were synthesized by the boiling citrate method.^{19,20} For stability against aggregation, 100 mg of bis(*p*-sulfonatophenyl)phenylphosphine dihydrate dipotassium salt (BSPP) was added to 100 mL of as-synthesized nanoparticles.^{21,22} The mixture was left to stir overnight (12–16 h), and excess reagents were removed by two centrifugation cycles (3000 RCF, 20 min). For 4,4'-dipyridyl complexation, 1 mL of 10 mM 4,4'-dipyridyl in water was added to 9 mL of BSPP-stabilized gold nanoparticles and left to complex overnight.²³ Excess reagents were removed by two centrifugation cycles (3000 RCF for 20 min). For final purification, we dialyzed the solutions in Thermo Scientific G2 Slide-A-Lyzer G2 cassettes against 4 L of Barnstead E-Pure (18 MΩ cm) water for 48 h.

■ AUTHOR INFORMATION

Corresponding Author

*E-mail: carney@uiuc.edu.

Notes

The authors declare no competing financial interest.

■ ACKNOWLEDGMENTS

The work was supported in part by the Beckman Fellows program. S.T.S. and B.M.D. acknowledge support from the University of Illinois at Urbana-Champaign from the NIH National Cancer Institute Alliance for Nanotechnology in Cancer “Midwest Cancer Nanotechnology Training Center” Grant R25CA154015A. M.V.S. acknowledges support through the Congressionally Directed Medical Research Program Postdoctoral Fellowship BC101112. We also acknowledge support from a Beckman Institute seed grant, AFOSR Grant No. FA9550-09-1-0246, and NSF Grants CHE-1011980 and CHE-0957849.

■ REFERENCES

- (1) Schatz, G. C.; Van Duyne, R. P. *Handbook of Vibrational Spectroscopy*; John Wiley & Sons: Chichester, U.K., 2002; Vol. 1, pp 759–774.
- (2) Lyandres, O.; Yuen, J. M.; Shah, N. C.; van Duyne, R. P.; Walsh, J. T.; Glucksberg, M. R. Progress Toward an In Vivo Surface-Enhanced Raman Spectroscopy Glucose Sensor. *Diabetes Technol. Ther.* **2008**, *10*, 257–265.
- (3) Qian, X.; Peng, X.-H.; Ansari, D. O.; Yin-Goen, Q.; Chen, G. Z.; Shin, D. M.; Yang, L.; Young, A. N.; Wang, M. D.; Nie, S. In Vivo Tumor Targeting and Spectroscopic Detection with Surface-Enhanced Raman Nanoparticle Tags. *Nat. Biotechnol.* **2008**, *26*, 83–90.
- (4) von Maltzahn, G.; Centrone, A.; Park, J.-H.; Ramanathan, R.; Sailor, M. J.; Hatton, T. A.; Bhatia, S. N. SERS-Coded Gold Nanorods as a Multifunctional Platform for Densely Multiplexed Near-Infrared Imaging and Photothermal Heating. *Adv. Mater.* **2009**, *21*, 3175–3180.
- (5) Frontiera, R. R.; Henry, A.-I.; Gruenke, N. L.; Van Duyne, R. P. Surface-Enhanced Femtosecond Stimulated Raman Spectroscopy. *J. Phys. Chem. Lett.* **2011**, *2*, 1199–1203.
- (6) Larmour, I. A.; Argueta, E. A.; Faulds, K.; Graham, D. Design Consideration for Surface-Enhanced (Resonance) Raman Scattering Nanotag Cores. *J. Phys. Chem. C* **2012**, *116*, 2677–2682.
- (7) Stone, N.; Faulds, K.; Graham, D.; Matousek, P. Prospects of Deep Raman Spectroscopy for Noninvasive Detection of Conjugated Surface Enhanced Resonance Raman Scattering Nanoparticles Buried within 25 nm of Mammalian Tissue. *Anal. Chem.* **2010**, *82*, 3969–3973.
- (8) Cao, Y. C.; Jin, R. C.; Nam, J. M.; Thaxton, C. S.; Mirkin, C. A. Raman Dye-Labeled Nanoparticle Probes for Proteins. *J. Am. Chem. Soc.* **2003**, *125*, 14676–14677.
- (9) Bharadwaj, P.; Novotny, L. Spectral Dependence of Single Molecule Fluorescence Enhancement. *Opt. Express* **2007**, *21*, 14266–14274.
- (10) Talley, C. E.; Jackson, J. B.; Oubre, C.; Grady, N. K.; Hollars, C. W.; Lane, S. M.; Huser, T. R.; Nordlander, P.; Halas, N. J. Surface-Enhanced Raman Scattering from Individual Au Nanoparticles and Nanoparticle Dimer Substrates. *Nano Lett.* **2005**, *5*, 1569–1574.
- (11) Kodali, A. K.; Llora, X.; Bhargava, R. Optimally Designed Nanolayered Metal-Dielectric Particles as Probes for Massively Multiplexed and Ultrasensitive Molecular Assays. *Proc. Natl. Acad. Sci. U.S.A.* **2010**, *107*, 13620–13625.
- (12) Jackson, J. B.; Westcott, S. L.; Hirsch, L. R.; West, J. L.; Halas, N. J. Controlling the Surface Enhanced Raman Effect via the Nanoshell Geometry. *Appl. Phys. Lett.* **2003**, *82*, 257–259.
- (13) Alvarez-Puebla, R. A. Effects of the Excitation Wavelength on the SERS Spectrum. *J. Phys. Chem. Lett.* **2012**, *3*, 857–866.
- (14) Bohren, C. F.; Huffman, D. R. *Absorption and Scattering of Light by Small Particles*; Jon Wiley and Sons: New York, 1983.
- (15) van de Hulst, H. C. *Light Scattering by Small Particles*; Dover Publications: Mineola, NY, 1982.
- (16) Bohren, C. F. Applicability of Effective-Medium Theories to Problems of Scattering and Absorption by Nonhomogeneous Atmospheric Particles. *J. Atmos. Sci.* **1986**, *43*, 468–475.
- (17) Johnson, P. B.; Christy, R. W. Optical-Constants of Noble-Metals. *Phys. Rev. B* **1972**, *6*, 4370–4379.
- (18) Kerker, M.; Wang, D. S.; Chew, H. Surface Enhanced Raman-Scattering (SERS) by Molecules Absorbed at Spherical-Particles: Errata. *Appl. Opt.* **1980**, *19*, 4159–4174.
- (19) Ji, X.; Song, X.; Li, J.; Bai, Y.; Yang, W.; Peng, X. Size Control of Gold Nanocrystals in Citrate Reduction: The Third Role of Citrate. *J. Am. Chem. Soc.* **2007**, *129*, 13939–13948.
- (20) Kimling, J.; Maier, M.; Okenve, B.; Kotaidis, V.; Ballot, H.; Plech, A. Turkevich Method for Gold Nanoparticle Synthesis Revisited. *J. Phys. Chem. B* **2006**, *110*, 15700–15707.
- (21) Loweth, C. J.; Caldwell, W. B.; Peng, X. G.; Alivisatos, A. P.; Schultz, P. G. DNA-Based Assembly of Gold Nanocrystals. *Angew. Chem., Int. Ed.* **1999**, *38*, 1808–1812.
- (22) Schmid, G.; Lehnert, A. The Complexation of Gold Colloids. *Angew. Chem., Int. Ed. Engl.* **1989**, *28*, 780–781.
- (23) Lim, D. K.; Jeon, K. S.; Hwang, J. H.; Kim, H.; Kwon, S.; Suh, Y. D.; Nam, J. M. Highly Uniform and Reproducible Surface-Enhanced Raman Scattering from DNA-Tailorable Nanoparticles with 1-nm Interior Gap. *Nat. Nanotechnol.* **2011**, *6*, 452–460.